

Research and Application of Materials Science

Editor-in-Chief: Zidong Wang

Associate Editors: Ting Zhu Junfei Ou Jing Wang

Editorial Board Members:

Zhongyi He	Yong Tian	Chunjuan Cui	Wenzhu Liu	Zesong Wang
Liwen Pan	Shuoping Chen	Zunli Mo	Chaogui Tan	You Wang
Qingyan Xu	Lizhao Qin	Wenlong Zhou	Shuquan Liang	Jinping Xiong
Shifa Wang	Donghong Wang	Yunping Li	Sheng Han	Xiehong Cao
Chunyan Li	Zhimin Wu	Mingchun Zhao	Xiaogang Han	Haihui Chen
Changsheng Liu	Jiangyong Wang	Dongjian Shi	Yanxin Qiao	Weixia Dong
Fazhan Wang	Zongrui Liu	Xiaoming Li	Lihua Zhu	Manfeng Gong
Shidong Zhu	Huanggen Yang	Jizhong Song	Xifeng Ding	Yongfeng Shen
Shengjun Lu	Zexing Wu	Wenli Gao	Xianyou Wang	Hui Sun
Mengnan Qu	Yandong Wang	Quanbing Liu	Qing Wang	Hongxu Li
Aokui Sun	Zhiguo Wang	Dilong Liu	Wanqing Song	Kai Liu
Wei Liu	Ying Li	Shaohua Luo	Suyun Tian	Zhinan Yang
Honglin Gao	Kongyin Zhao	Jiangmiao Yu	Xiaowei Zhang	Zhichao Lou



Publisher: Viser Technology Pte. Ltd.

ISSN: 2661-4464(online)

2661-4456(print)

Frequency:Semi-annual

Add.:21 Woodlands Close, #08-18

Primz Bizhub SINGAPORE (737854)

<https://www.viserdata.com/>

Editors:

Yajun Lian Yanli Liu

John Wilson Nike Yough

Mart Chen Qiuyue Su

Debra Hamilton Xin Di

Jennifer M Dohy Xiuli Li

Edward Adam DavisLiangjun Qiu

Designer: Anson Chee

Research and Application of Materials Science

Volume 3 No.1 (2021)

CONTENTS

- Development of a Rapid Test Bar for Quantitative Detection of Chloride Ions in Fresh Concrete..... 1**
Yingjie ZHANG, Shujie WEI, Wen PAN, Xuping JI, Zijian SONG
- Coal Based Carbon Dots for Fe³⁺ Detection and Photoelectric Catalysis 8**
Jianzhe JIANG, Zheng WANG, Shangwen MA, Gengxiong A, Ruiqi FENG, Tiezhen REN
- Monodisperse SiO₂ Microspheres with Large Specific Surface Area: Preparation and Particle Size Control 17**
Shengkai LI, Xianjin XU, Wei LI, Lei WANG, Haijin NING, Shengliang ZHONG
- B, N-Co-doped Carbon Tubes with P Encapsulated in 3D Graphene Aerogel for High-stable Lithium-ion Batteries
..... 24**
Fengfeng XU, Jian LIN, Cuiyan TONG, Haizhu SUN
- Synthesis and Mechanical Properties of C/PLA 3D Printing Composites Based on Waste Rice Noodles 30**
Jie YANG, Xinyan JIN, Yan LIU, Shuoping CHEN
- A Novel Preparation Method of Organic-inorganic Aramid Nanofibers (ANFs) Hybrid Membrane Using Ethanol
as Proton Donor 34**
Shengjun LU
- Gradient Ultra-fine Grained Surface Layer in 6063 Aluminum Alloy Obtained by Means of Rotational Accelerated
Shot Peening 38**
Ying LIU, Hailu XU, He XIAN, Yanfang LIU, Zheng LI

Development of a Rapid Test Bar for Quantitative Detection of Chloride Ions in Fresh Concrete

Yingjie ZHANG^{1,2}, Shujie WEI², Wen PAN², Xuping JI^{1,2}, Zijian SONG^{2*}

1 State Key Laboratory of High Performance Civil Engineering Materials, Nanjing 210098, China

2 College of mechanics and materials, Hohai University, West Focheng Road 8#, Nanjing, 211100, China

*Corresponding Author: Zijian SONG, E-mail: West Focheng Road 8#, Nanjing, 211100, China songzijian@hhu.edu.cn

Abstract:

Due to the shortage of natural raw materials, many practitioners proposed to make concrete from desalinated sea sand. To reduce the risk of abuse of uncleaned sea sand, we proposed a new rapid test bar to detect chloride ions in fresh concrete quantitatively. The test bars were prepared by mixing silver chromate with cotton fiber. By virtue of the high liquid-absorbent capacity of cotton fiber, the chloride-contained liquid in fresh concrete will rapidly enter into the test bar and react with the silver chromate to finally show a certain coloring height, which corresponds to the actual chloride content. In order to optimize the preparation process, the color rendering, testing time and stability of test rods under different mixing ratios and conditions were investigated. The relationship between color height and chloride content was established, and an auxiliary card is prepared for user-friendly calculation of chloride content. The results showed that the best performance of the test bar was obtained under the following conditions: mass concentration of silver chromate 5.0g/L, soaking time 1 min, drying temperature 50 °C and content of discolored silica gel 0.5g/ root.

Keywords: Test bar; Chloride ion; Concrete; Cotton fiber

1 Introduction

Since the emergence of reinforced concrete structures in 1880 and their application in industrial buildings, concrete materials have become indispensable materials in civil construction engineering because of their broad applicability and low cost^[1-2]. China is currently in the peak period of infrastructure construction and maintenance, and is the area where reinforced concrete structures are most used in the world. However, the safety and durability of reinforced concrete structures cannot be ignored. Affected by the destruction of the concrete itself and the surrounding environment, a large number of early concrete structures suffer from disease and degradation under the condition of not reaching their service life, which leads to premature failure of the structure and causes enormous direct and indirect losses. Corrosion of steel bars is one of the causes of poor durability of concrete structures. Economic losses and maintenance costs caused by corrosion of steel bars are extraordinary^[3-5]. According to the investigation results of corrosion by Academician Hou^[6], the annual economic losses caused by corrosion in China is account for about 3.34% of the GDP. It can be seen that the

durability of concrete caused by corrosion of steel bars is a significant problem that should be widely concerned by all countries in the world. In modern engineering construction, concrete will still be one of the largest building materials^[7], and the durability of reinforced concrete is the fundamental guarantee to ensure the safe operation of all kinds of projects, which is a common concern and necessary research problem at home and abroad. In this context, it is very important and far-reaching to carry out the research on the measures to improve the durability of reinforced concrete to prolong the service life of reinforced concrete structures and ensure the safe operation of all kinds of engineering facilities.

At present, chloride corrosion is the main cause of steel corrosion^[8]. Chloride ion has a small radius and strong permeability. The pH value here is significantly reduced, when chloride ion penetrates the passivation film on the steel bar surface and adsorbs on the steel bar surface^[9]. Recent theoretical developments have revealed that^[10], when the pH value is less than 11.5, the passivation film will become unstable. When the pH value is less than 9.88, the passivation film starts to be destroyed, and no new passivation film is formed. When the passivation film is damaged, it will no longer play a protective role in the steel bar, and when the O₂ and H₂O

come into contact with the steel bar, the steel bar will rust^[11]. Moreover, the Cl⁻ also has a transport function^[12]. Cl⁻ reacts with Fe²⁺ to form FeCl₂, and then FeCl₂ dissolves in water to form Fe(OH)₂ precipitation when it encounters OH⁻. When Fe(OH)₂ diffuses into the concrete, it forms iron oxide and rust, leading to steel bars' corrosion. In this process, Cl⁻ is not consumed, which plays the role of "catalytic transport" and accelerates the corrosion of steel bars exponentially. Currently, many areas are facing a shortage of sand and gravel, some areas have begun to use sea sand resources. China is rich in sea sand resources, with a reserve of 16,000 tons of sea sand. As we all know, sea sand containing too many chloride ions have strong corrosivity^[13-15]. Song Xuyan et al.^[16] showed that if sea sand is directly used to prepare concrete, the high chloride ion content of sea sand will accelerate the corrosion of steel bars in concrete. Once untreated seawater is used in concrete buildings, it will inevitably cause the corrosion of steel reinforcement in the concrete and the decline of concrete durability, which will cause the destruction of buildings. 60%~70% of the sand used for concrete production in Guangzhou is desalinated sea sand or sand mixed with river sand^[17]. At present, river sand resources in China are becoming scarce lacking, and inappropriate use of sea sand leads to the problem of "sea sand house"^[18].

If the content of chloride ions in concrete can be controlled, the problem of steel corrosion can be alleviated, so as to improving the durability of reinforced concrete and prolong the service life of reinforced concrete structures. Therefore, detecting chloride ions in fresh concrete has become an indispensable part of modern engineering^[19]. Moreover, China already has the standard stipulation of chlorine ion detection technology in concrete^[20]. At present, the commonly used detection methods include silver nitrate titration, chloride ion selective electrode method and paper colorimetry. The method of silver nitrate titration depends on the change of color, which is easy to cause error^[21]. Although chlorine ion selective electrode method can accurately detect the content of chlorine ion, it has the disadvantages of poor portability. Barriers for testers are high and time consuming. The use of paper colorimetry will cause visual errors. Therefore, we develop a test bar for the detection of chlorine ions in fresh concrete. Once we directly insert the test bar into the fresh concrete, the degree of discoloration indicates the amount of chloride ion in the concrete with portability, rapidity and accuracy. Furthermore, it provides a simple, accurate and rapid detection method for engineering supervision and detection. Convenient, efficient and rapid chloride ion content detection provides a guarantee of improving the project quality and reducing the project risk, thus stabilizing the quality of engineering concrete products and improving the durability of concrete.

2 Experimental section

2.1 Materials and reagents

Pure potassium chromate (analysis), silver nitrate (analysis), sodium chloride (analysis), cotton fiber, silica gel, water color silicone, poly carboxylic acid water reducing agent (Nanjing TongXin technology co., LTD.), acrylic plastic pipe (TianChang organic products co., LTD.), cement (Portland cement), sea sand (apparent density of 2480 kg/m³) and limestone rubble (5 ~ 25 mm continuous gradation, apparent density of 2650 kg/m³) were used in this experiment to preparation the test bars and the samples.

2.2 Instruments and equipment

Electric blast dryer (sbk-101A-3, Nanjing sibeke instrument co., LTD.), electronic balance (wtb-5003, Hangzhou wante co., LTD.), filling mold (Nanjing TongXin technology co., LTD.), mixer (Shanghai QiuZuo instrument co., LTD.) and camera (SAMSUNG-NSmini) were used in this experiment.

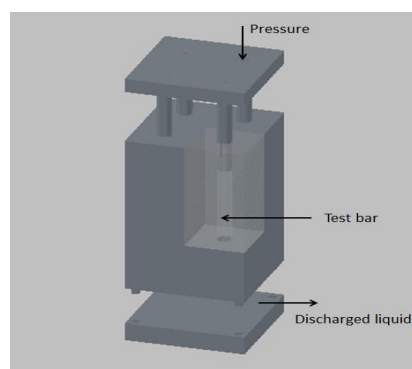


Figure 1 Application method of filling mold

2.3 Experimental principle

Cotton fiber and absorbent silica gel excel in water absorption. They can absorb the pore solution in the newly mixed concrete into the test bar. Under certain conditions, silver chloride precipitation is generated by silver chromate reacting with chloride ions. Within a certain range, the content of chlorine ions is proportional to the height of white precipitation. By comparing the height of rise with a standard height card, the mass concentration of chlorine ions can be determined, therefore, the content of chlorine ion in fresh concrete can be quantitatively detected.

2.4 Experimental methods

2.4.1 Preparation of test bar

First, we prepared silver chromate solution with a mass concentration of 5g/L and put 300 mL (of the solution) into a beaker. Then, the cotton fiber and absorbent silica gel were immersed in the solution for 1 min adding polycarboxylic acid water reducer. Third, the

agitator stirred the fiber for 10 minutes at 1000 RPM, in order to make a composite base core of the cotton fiber. After 3 minutes of vibration to remove most of the water, it was placed in a blast drying box and dried at a specific temperature. The color-changing silica gel powder was applied to the upper end of the test bar with the coating amount of 0.5g/root when it was dry. The prepared test bar should be stored in a vacuum bag in a dry and closed place away from light.

2.4.2 Selection of test bar preparation parameters

Portland cement was used to prepare concrete samples in this experiment. By changing the preparation parameters such as the content of cotton fiber, the length of test bar, the drying temperature, etc., test bars with different parameters were prepared and put into the fresh concrete pore solution. The absorption time, color effect and color contrast were then observed to determine the preparation parameters of the test bar. 2.4.3. The preparation of corresponding cards

The test bars were prepared at 25°C and inserted into the concrete pore solution with chloride ion content of 0.005%, 0.01%, 0.02%, 0.03%, 0.04%, 0.05%, 0.06%, 0.07%, 0.08%, 0.09% and 0.10%, respectively. The height of the color-changing part of the test bar was detected after the color change was stabilized, and the relationship card of "color-changing height of the test bar - chloride ion concentration" was prepared according to the experimental results.

2.4.3 Test bar stability test

Temperature stability test

According to the adjusted parameters, the test bars were prepared to test the chloride ion content in C25, C30 and C40 fresh concrete at 5°C, 15°C, 25°C and 35°C, respectively, to verify the temperature stability.

Reproducibility experiment

The adjusted parameters were divided into 6 batches to prepare the test bars. The test bars were selected from each batch to test the chloride ions in 5 different pore solutions of fresh concrete, to verify the repeatability of the results of multiple measurements.

Coexisting ion effect

Coexisting ions with different contents were added into C30 concrete pore solution with chloride ion concentration of 0.06% and tested with chloride ion test bars. The test results were compared with the standard height to verify the anti-jamming ability of the test bar.

3 Results and discussion

3.1 Influence of preparation parameters on water absorption and color contrast

Test bars at different temperatures were dried to investigate the effect of drying temperature on the color development effect of the test bar. Photos were taken to read RGB values in the color panel by Photoshop, as shown in table 1. The color rendering effect of the test bars dried at different temperatures was different. The

color rendering contrast of the low-temperature drying bars was obvious but took a longer time. With the increase of temperature, the drying time of the test bar is shortened. However, the color contrast of the test bar is no longer obviously apparent. Taking color contrast and drying time into consideration, the paper was prepared by blast drying at 50°C.

During the experiment, the content of cotton fiber has a significant influence on the water absorption of the test bar, and the selection of the base core of the test bar should meet the requirements of absorbing pore solution easily and large capacity. As can be seen from Table 2, the adsorption effect differed with the addition of different amounts of cotton fibers. The adsorption rate is defined as the ratio of the density after water absorption to the density before water absorption. When the cotton fiber incorporation amount is small, it is easier to absorb the pore solution, but the total adsorption amount is small. When the content of cotton fiber is about 1.5g/cm³, the adsorption of the pore solution is relatively easy, and the total adsorption capacity is significantly increased. When the content of cotton fiber is increased gradually, the total adsorption is increased slightly, but the adsorption of pore solution became more difficult. Considering the factors such as the difficulty of absorbing pore solution and the total adsorption capacity, the cotton fiber content was 1.5g/cm³.

Table 1 Influence of drying temperature on color rendering effect of test bar







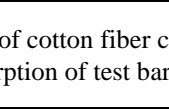
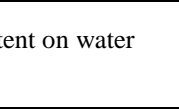
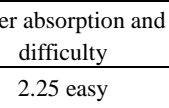
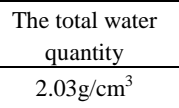
Dry conditions	Drying time	Pre-reaction color	Post-reaction color
30°C Drum wind drying	8h		
40°C Drum wind drying	6.5h		
50°C Drum wind drying	5h		
60°C Drum wind drying	3.5h		
70°C Drum wind drying	2h		

Table 2 Influence of cotton fiber content on water absorption of test bar

Cotton fibre content	Water absorption and difficulty	The total water quantity
0.9g/cm ³	2.25 easy	2.03g/cm ³
1.2g/cm ³	2.03 easy	2.43g/cm ³
.5g/cm ³	1.95 normal	2.92g/cm ³
1.8g/cm ³	1.83 difficult	3.22g/cm ³
2.1g/cm	1.65 hard	3.30g/cm ³

During the use of the test bar, the length of the test bar has a significant influence on the measuring range of the test bar and the adsorption time of pore solution. The

selection of the length of the test bar should meet the requirements of a shorter adsorption time of pore solution and wider measurement range. Twelve kinds of test bars in different lengths were prepared, and 4 rods of each type were selected for the adsorption time test and the results were averaged. With the increase of the length of the test bar, the detection ranges of chlorine ions in the fresh concrete increases, but the time to fully absorb the pore solution also increases gradually. It can be seen from table 3 and Figure 2 that the adsorption time of the test bar for pore solution increases with the augment of the length of the test bar and the increment of time tardily. The specification requires that the maximum chloride ion content in concrete is 0.06%. As can be seen from Figure 3, when the length of the test bar is less than 40mm, the adsorption time of pore solution is shorter, but the measurement range is smaller. When the length of the test bar is more than 55 mm, the measurement range continues to increase, but the adsorption time of the pore solution is increased significantly. Combined with the approximate range of chlorine ion content in fresh concrete and the actual construction detection time, the length of the test bar should be selected as 50 mm. As shown in Figure 4, test bars were inserted into freshly mixed concrete, and every 3-test bar was a group. After completion of detection, the test bars were removed and the average value of the three test bars was recorded.

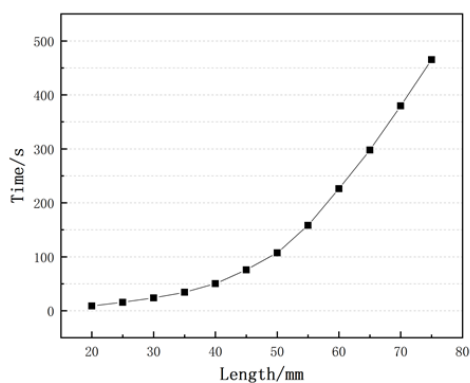


Figure 2 Relationship between the length of test bar and the service time of test bar

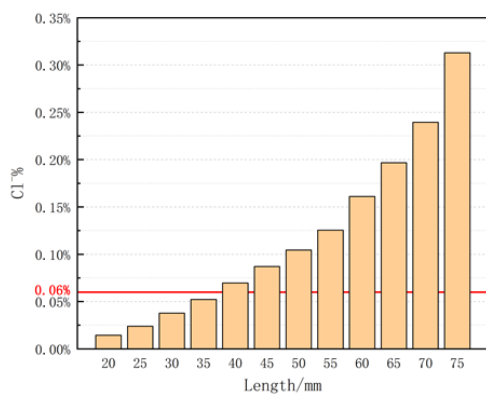


Figure 3 Relationship between the length of test bar and the range of test bar



Figure 4 Test method for test bar in freshly mixed concrete

Table 3 Influence of length on the time and range of test bar

Length /mm	Time/s	Maximum range (percentage chloride weight)
20	8.91	0.0145%
25	15.73	0.0239%
30	23.78	0.0377%
35	34.18	0.0522%
40	50.09	0.0696%
45	75.78	0.0871%
50	107.35	0.1045%
55	158.23	0.1255%
60	226.18	0.1611%
65	297.65	0.1967%
70	379.47	0.2395%
75	465.26	0.3129%

3.2 Relationship between the color change height of test bar and the content of chlorine ion

Under the same condition, the test bars with adjusted parameters were placed into the concrete pore solution with different design concentrations in turn. The color change height of each test bar was recorded after 120 s of absorption. According to different chloride ion concentration and corresponding color rendering height of the test bar, the "color rendering height - chloride ion content" curve was fitted, as shown in Figure 5, Figure 6 and equations (1), (2). With the increase of chloride ion content, the color rendering height of the test bar also increased significantly. As shown in Figure 7, the corresponding card of "color development height - chloride ion content" was drawn according to the index value of test bar, so as to realize the semi-quantitative and rapid detection of chlorine ion content in the pore solution of fresh concrete.

Table 4 Different chloride ion concentration and corresponding color developing height of test bar

Cl-%	Length/mm
0	0
0.005	10
0.01	17
0.02	23
0.03	27
0.04	31

Cl%	Length/mm
0.05	34
0.06	37
0.07	40
0.08	43
0.09	46
0.1	49

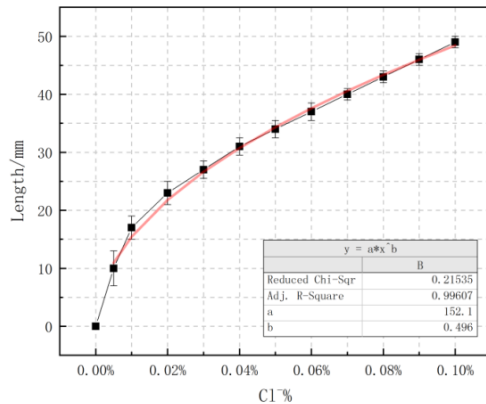


Figure 5 Fitting curves of different chloride ion concentrations and corresponding chromogenic heights

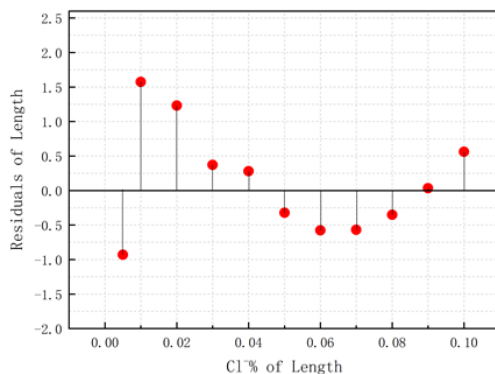


Figure 6 Residuals of color rendering length

$$Y = 152.1X^{0.496} \quad (1)$$

$$X = \sqrt[0.496]{\left(\frac{Y}{152.1}\right)} \quad (2)$$

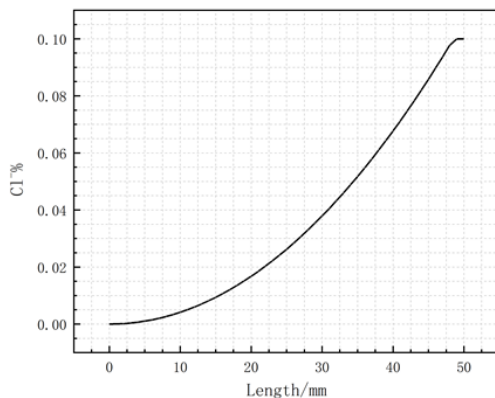


Figure 7 "Color development height - chlorine ion content" corresponding curve

Table 5 "Color development height - chlorine ion content" corresponding card

Length/mm	Cl%	Length/mm	Cl%	Length/mm	Cl%
0	0.0000	18	0.0135	35	0.0517
2	0.0002	19	0.0151	36	0.0547
3	0.0004	20	0.0167	37	0.0578
4	0.0007	21	0.0185	38	0.0610
5	0.0010	22	0.0203	39	0.0643
6	0.0015	23	0.0222	40	0.0677
7	0.0020	24	0.0242	41	0.0711
8	0.0026	25	0.0262	42	0.0747
9	0.0033	26	0.0284	43	0.0783
10	0.0041	27	0.0306	44	0.0820
11	0.0050	28	0.0330	45	0.0858
12	0.0060	29	0.0354	46	0.0897
13	0.0070	30	0.0379	47	0.0937
14	0.0082	31	0.0405	48	0.0978
15	0.0094	32	0.0432	49	0.1000
16	0.0107	33	0.0459	50	0.1000
17	0.0121	34	0.0488		

3.3 Stability analysis

3.3.1 Temperature stability

The content of chloride ion in C25, C30 and C40 fresh concrete was measured with test bars in the case of changing the ambient temperature. As can be seen from Table 6, the test of C25, C30, and C40 fresh concrete at 5°C, 15°C, 35°C was carried out by the test bar and the deviation of the measured value at 25°C was within ± 10% at different temperatures, which indicated this method was not sensitive to temperature and could be applied to a variety of temperature environments. The indicator number of the test bar did not change significantly with the increase of temperature, which was similar to that of the potentiometric titrator at different temperatures. This may be due to the fact that the reaction process of silver chromate combined with chloride ions in the indicator material to generate silver chloride was not susceptible to environment temperature. Moreover, temperature compensation can be provided at lower ambient temperatures due to the heat released during cement hydration. When testing bars used in a higher temperature environment, moisture of the fresh concrete evaporated faster with the increase of ambient temperature, consequently the concentration of the sodium chloride in concrete increased slightly. Likewise, the absorption volume of the test bars was unchanged and the concentration of chloride ion increased, resulting in the index of the test bars slightly higher than normal temperature environment (25°C). The evaporation of concrete moisture was negligible at relatively high temperatures due to the short time used by the test bars, thus the influence of

temperature on the measurement results could be ignored. Therefore, the change of environmental temperature had little interference to the test bars in engineering applications. The evaporation of moisture could be negligible in a short time at room temperature, while it was necessary to control the mixing time of concrete to suppress the evaporation in a high temperature environment.

3.3.2 Reproducibility

Under the same environment, test bars made in six different batches were put into five kinds of fresh concrete. The data results and deviations are shown in table 7. When the chloride ion concentration is small, the variance of data is small, but the gap between each batch is still large, so the error in measuring the mixed concrete with low chloride ion concentration is large. It can be seen from table 7 that for the same sample, although some data deviate greatly, the test results are all very close. As an example, the difference between the test results of sample No. 2 with a maximum deviation of 0.00376 is only 0.0083% of the chloride ion content, indicating that the difference in results is not significant. At the same time, the reserved number of the decimal point also greatly influences the calculation of the deviation. For example, if the last two digits of a small number are accurate to the percentage, the two data records will become 0.02% and 0.02%, and the deviation will be 0.

3.3.3 Influence of coexisting ions

It can be seen from Table 5.6 that with the increase of the content of SO_4^{2-} , Mg^{2+} and CO_3^{2-} ions commonly found in concrete in fresh concrete, the number of test bars is relatively stable without major fluctuations. Therefore, SO_4^{2-} and CO_3^{2-} ions do not affect the test results of rapid test bars. The principle of color development of the indicator material is the combination of silver chromate and chloride ions to form silver chloride. Under the same temperature environment, the solubility product of silver chromate is less than that of silver sulfate, silver carbonate and other substances, and is greater than that of silver chloride. Therefore, in the

complex ion environment of the concrete itself, the indicating material in the detection test rod can "avoid" the carbonate sulfate radical plasma to preferentially react with the chloride ion to complete the detection of the chloride ion in the fresh concrete. When the traditional silver nitrate titration method is used to detect the chloride ion in concrete, the sulfate and carbonate ions contained in the method need to be removed in advance. The process is complex and the anti-interference ability is weak. Compared with the traditional method, the rapid detection test bar method has good anti-interference performance in concrete. The addition of iodine ion in fresh concrete will greatly affect the indicator of test rod. With the increase of iodine ion content in fresh concrete, the indicator of test rod will also increase significantly. This is because the indicator material is more likely to bind iodine ions and can only bind chloride ions in the solution of the inhalation hole, thus, the rapid detection test rod is not suitable for detection under the condition of containing halogen group element ions. In summary, since the halogen group element ion content is less in the concrete, the rapid detection test bar has a good resistance to ion interference.

4 Conclusion

A novel method based on concrete test bar was established to detect the concentration of chlorine ion swiftly and optimized its conditions of preparation process and formula. The influence of the preparation parameters on the test bar demonstrated that the test bars exhibited excellent performance under the best conditions (5.0 g/L silver chromate, soaking time 1 min, drying temperature 50°C). The test bar had the characteristics of small size, sensitive response, low cost, easy operation, and high stability. Moreover, the test bar could realize the rapid detection of semi-quantitative detection compared with the traditional method of silver nitrate titration. In general, it had a wide range of applications, great potential and development prospects in the construction industry.

Table 6 Test results of test bars at different ambient temperatures %

Strength grade	25°C		35°C		15°C		5°C	
	Measured value	Measured value	Deviation	Measured value	Deviation	Measured value	Deviation	
C25	0.0148	0.013794	-6.8	0.015599	5.4	0.015792	6.7	
C30	0.0254	0.026187	3.1	0.026543	4.5	0.027356	7.7	
C40	0.0185	0.017168	-7.2	0.020147	8.9	0.019888	7.5	

Table 7 Test results of different batches of test rods in concrete

Concrete number	First batch /%	Second batch /%	Third batch /%	Fourth batch /%	Fifth batch /%	Sixth batch /%	The variance
1#	0.0009	0.0014	0.0026	0.0007	0.0015	0.0033	0.00101
2#	0.0165	0.0212	0.0173	0.0239	0.0244	0.0161	0.00376
3#	0.0356	0.0335	0.0413	0.0359	0.0387	0.0364	0.00272
4#	0.0613	0.0635	0.0672	0.0624	0.0677	0.0618	0.00279
5#	0.0821	0.0867	0.0842	0.0821	0.0852	0.0841	0.00179

Table 8 Results of cross reaction of test bar to other ions

SO ₄ ²⁻	0.003%	0.006%	0.01%	0.02%	0.03%	0.04%
Color rendering height/mm	38	38	38	38	39	38
Mg ²⁺	0.003%	0.006%	0.01%	0.02%	0.03%	0.04%
Color rendering height/mm	38	38	38	38	39	39
I ⁻	0.003%	0.006%	0.01%	0.02%	0.03%	0.04%
Color rendering height/mm	39	39	41	44	46	49
CO ₃ ²⁻	0.003%	0.006%	0.01%	0.02%	0.03%	0.04%
Color rendering height/mm	38	38	38	38	38	38
Br ⁻	0.003%	0.006%	0.01%	0.02%	0.03%	0.04%
Color rendering height/mm	38	39	40	43	46	49

Conflict of Interest: The authors declare that there is no conflict of interest regarding the publication of this paper.

References

- [1] L Tian. General situation and some characteristics of durability research of Concrete Structures. *Construction Structure*. 1995; 12, 44-90.
- [2] Z J Cheng, D Song, J H Jiang, et al. Research progress on corrosion and Protection of reinforcement in concrete. *Thermal Processing Technology*. 2016, 45: 14-19.
- [3] S Z Xue. Deterioration and repair of concrete structures. *Tunnels and rail transit*. 2019: 1-4.
- [4] Y G Yu, W G A Castel, A R Liu, et al. Modelling steel corrosion under concrete non-uniformity and structural defects. *Cement and Concrete Research*. 2020: 135.
- [5] Z Y Li. Aging treatment of hydraulic concrete buildings. *Knowledge Economy*. 2009, 7: 186.
- [6] B.R. Hong, D. Zhang, P. Wang. Current situation and future of Marine corrosion protection. *Journal of Chinese Academy of Sciences*. 2016, 31, 1326-1331.
- [7] E R Grist, K A Paine, A Heath, et al. Structural and durability properties of hydraulic lime-pozzolan concretes. *Cement and Concrete Composites*. 2015: 62.
- [8] J W Bao, J N Wei, P Zhang, et al. Research progress on similarity of Concrete resistance to Chloride Ion erosion in Marine environment. *Journal of Silicate*. 2020, 48: 689-704.
- [9] K K Gao, W F Cui, P. Zhang, et al. Advances in research on corrosion of reinforced concrete induced by alkali under chloride erosion. *Bulletin of Silicate*. 2020, 6: 1-9.
- [10] H M Jia, G.P. Yan, G.J. Yan. Research on reinforcement corrosion in concrete. *Chinese Journal of Safety Science*. 2005, 5: 56-60.
- [11] W P Zhang, X L Gu, X Y Jin, et al. Study on corrosion mechanism and Mechanical properties of Corroded Reinforcement in concrete. *Journal of Building Structures*. 2010, 31: 327-332.
- [12] R G Du, Y Liu, C J Lin. Effect of chloride ion on corrosion mechanism of reinforcement and its research progress. *Material Protection*. 2006, 6: 45-133.
- [13] X J Li. Exploration and Utilization and Ownership Management of Marine sand resources at home and abroad. *Cooperative Economy and Science and Technology*. 2018, 24: 49-51.
- [14] F G Leng, W Ding, Y X Zhou, et al. Some Key points of Marine sand concrete application technology. *Construction technology*. 2011, 40: 97-100.
- [15] F He, J X Ji. Effect of sea sand on concrete durability and desalination treatment, *Cement engineering*. 2015, 4: 72-75.
- [16] X Y Song, Z P Jiang, J Y Han, et al. Study on reinforcement corrosion in sea sand concrete. *Concrete and cement products*. 2019, 9: 19-23.
- [17] J H Chen, W J Pan. Research on the determination method of Chloride ion content in fresh concrete. *Guangdong Civil and Architecture*. 2015, 22: 137-139.
- [18] N F Hong. Corrosion of sea sand and harm of "sea sand house". *Industrial Building*. 2004, 11: 65-67.
- [19] Y Q Li. Detection technology of chloride ion content in site premix concrete. *Construction machinery*. 2019, 7: 102-213.
- [20] L J Li. Chlorine ion mechanism in concrete and its detection technology. *Low carbon world*. 2019, 9: 323-324.
- [21] L T Hao, K L Luo, S X Zhang, et al. Determination of chlorine ions in natural water by ion selective electrode. *Journal of Inspection and Quarantine*. 2019, 29: 25-28.

Coal Based Carbon Dots for Fe³⁺ Detection and Photoelectric Catalysis

Jianzhe JIANG¹, Zheng WANG², Shangwen MA³, Gengxiong A³, Ruiqi FENG¹, Tiezhen REN^{1*}

1. School of Chemical Engineering, Hebei University of Technology, Tianjin 300130, China.

2. State Key Laboratory of High-efficiency Utilization of Coal and Green Chemical Engineering, Ningxia University, Yinchuan 750021, Ningxia, China

3. Bayingol vocational and technique school, Korla 84100, Xinjiang, China

*Corresponding author: Tiezhen REN, E-mail: rtz@hebut.edu.cn

Abstract:

The carbon dots (CDs) could be applied in advanced field by using their sensitivity of the optical phenomenon. In this paper, the CDs in an average size of 3.75 nm was synthesized from coal by one-step solvothermal method, in which ethylenediamine was a reaction solvent and a nitrogen-containing precursor in the system. A blue-green fluorescence appeared under ultraviolet light. The strongest fluorescence emission was recorded at 480 nm under the excitation wavelength of 400 nm. The coal-based CDs could specifically recognize Fe³⁺ and the detection limit was 0.103 μM. The coal-based CDs/TiO₂ composite displayed an improved photoelectric response in 4 times comparing that of the TiO₂ under the ultraviolet light with intensity of 10 mW cm⁻². The photocatalytic activity over the degradation of organic molecules was accelerated as well.

Keywords: solvothermal; carbon dots; Fe³⁺ detection; photocurrent response; photodegradation

1 Introduction

Carbon dots (CDs) possess the unique optical properties, stable chemical properties, good bio-compatibility and excellent opto-electronic properties [1-2]. At present, carbon sources, such as graphite, carbon nanotubes, organic molecules and biomass material etc., have been applied for CDs preparation [3-6]. On the surface of the CDs the abundant functional groups can specifically recognize metal ions. The CDs from citric acid and melamine exhibited the Fe³⁺ detection limit around 142 nM [5]. CDs from citric acid and glycine represented the Fe³⁺ detection through the phenolic hydroxyl group [6].

On the other hand, CDs are composed the conjugated π structure, which can effectively improve the photocatalytic activity and photoelectric conversion in the visible light region. CDs modified TiO₂ nanoparticles (P25) in one-step hydrothermal technique were interconnected by Ti-O-C bonds and exhibited higher efficiency than the P25 powder for the photocatalytic hydrogen production [7].

Among the carbon sources of synthetic CDs, coal has unique advantages in terms of carbon content, large

reserves and low price [8-12]. The coal-based CDs were obtained through acid oxidation [8]. When mixed with TiO₂, they could effectively photodegrade organic pollutants under the sunlight and 81.2 % degradation could be achieved. The CDs with graphite microcrystal structure was obtained by the carbonization of coal and their sizes at 1.96 nm, 2.27 nm and 3.10 nm were controlled through chemically cutting coal. The sp² carbon domain structure and surface defects were responsible to the fluorescence emission [10]. The CDs by nitrification treatment of coal pitch and a solvent heat treatment displayed an orange fluorescence in aqueous solution [11]. While, the strong acid solution oxidation for CDs preparation caused the environment pollution seriously. It is still of great significance to explore more efficient preparation process to fulfill the large-scale preparation of CDs.

In this paper, we prepared fluorescent CDs from coal by one step solvothermal method in the absence of strong acid. The ethylenediamine was used as both the solvent and the nitrogen-containing precursor. The coal-based CDs represented a blue-green fluorescence under ultraviolet light and exhibited the strongest fluorescent emission peak at 480 nm at the optimal excitation wavelength of 400 nm, which was sensitive to

the detection of Fe^{3+} . In addition, the CDs-TiO₂ composite displayed an efficient photosensitivity, suggesting an excellent application of photosensitive material.

2 Experimental

2.1 Preparation of coal-based CDs for Fluorescence detection

All the precursors were used without pretreatment. 0.1 g of coal to 6 mL of absolute ethanol and 4 mL of ethylenediamine were mixed with stirring for 30 mins. The mixture was then transferred to a Teflon-lined reactor and kept at 180 °C for 12 h. After cooling to the room temperature the obtained solution was subjected to rotary evaporation to remove excess solvent and then purified through a 0.22 micron filter. The final product was dried it at 150 °C for collecting the CDs powder. A solution in 0.5 mg mL⁻¹ with absolute ethanol was prepared with CD powder and named as MCD64. The same protocol was used according to different ratios of ethanol and ethylenediamine solvent, and the related solution were named MCD100, MCD82, MCD55, MCD010, respectively. The control experiment was carried out without adding coal and the sample was named CD64. The pH of of the final solution was about 7. To investigate the fluorescence, we took 3 mL of CDs solution mixed with 1 mL of different ion solution. The NaCl water solution in pH range of 1-14 was adjusted by HCl (1 M) or NaOH (1 M). The metal ion solution in 5 μM (Ba^{2+} , Fe^{3+} , Ni^{2+} , Cu^{2+} , Mn^{2+} , Cr^{3+} , Co^{2+} , Zn^{2+} , K^+ , Mg^{2+} , and Na^+) were tested under the same conditions. All these solution system was standing at room temperature for 5 minutes and then the fluorescence emission spectrum was measured at an excitation wavelength of 400 nm.

2.2 Characterizations

The UV-vis absorption spectrum was collected with the TU1901 equipment and BaSO₄ was used for calibration. An Edinburgh Instrument FSP920 was used to record the fluorescence spectrum at room temperature. The transmission electron microscopy (TEM, JEOL JEM-2100F) recorded the morphology and size at 200 kV by dispersing the sample on the copper grid covered with carbon film. The structure of the sample was measured on X-ray diffraction (XRD, Bruker D8 Advance diffractometer) with Cu radiation ($\lambda = 0.154$ nm) and the 2θ range was set from 5 to 80 °. The Fourier transform infrared (FTIR) spectra were carried out on a Bruker VERTEX 70 instrument with KBr tablet. The carbon surface chemistry of CDs was recorded by the X-ray photoelectron spectra (XPS, Physical Electronics PHI 5000 Versa Probe II spectrometer). The sample chamber was irradiated by a monochromatic Al K α radiation (50 W, 15 kV, 1486.6 eV) after evacuated to 5.2×10^{-9} mbar. The C1s photoelectron line at 284.8 eV was used to calibrate the spectrometer energy scale. To

determine the binding energy of different element core energy levels accurately, the deconvolution was performed with Gauss-Lorentz model.

2.3 Preparation and performance of MCD64/TiO₂ composite photoelectric materials

2 ml of MCD64 (0.5 mg mL⁻¹) was mixed with 8 ml of distilled water, followed by addition of 100 mg of TiO₂ powder at room temperature for 2 hours to obtain a homogeneous suspension. The suspension was then transferred to a 30 mL stainless steel Teflon reactor and held at 140 °C for 4 hours. After cooling to room temperature, the obtained product was centrifuged at 3000 rpm for 10 minutes to collect a solid sample, which was washed twice with absolute ethanol, and finally dried at 50 °C to obtain MCD64/TiO₂ complex. Then its uniform suspension was prepared with ethanol and evenly coated on the ITO conductive glass within an effective area of 2 cm². Subsequently, the membrane was dried in a constant temperature oven at 150 °C for 30 minutes to increase the adhesion of the surface. This ITO glass covered with MCD64/TiO₂ was used as the working electrode for the investigation of the photocurrent response. Photoelectric response was tested with IM6&ZENNIUM (Zahner) electrochemical workstation and UV light emitting diode (UVR01, 390 nm) with intensity of 10 mW cm⁻². The working electrode of ITO glass was assembled in a three-electrode system with Pt as a counter electrode and Ag/AgCl as a reference electrode. 0.2 M of Na₂SO₄ solution was used as the electrolyte. The Electrochemical impedance spectroscopy (EIS) was evaluated with the frequency range from 10 mHz to 30 kHz with a perturbation amplitude of 5 mV.

3 Results and discussion

3.1 Fluorescence properties of prepared coal-based CDs under different systems and detection of metal ions

The CDs were formed with the ratio change of ethanol and ethylenediamine, in which the coal powder was the basic materials. The sample represents blue color under daylight and light yellow color under UV-light (Figure 1a). MCD64 has the strongest fluorescence intensity at 480 nm among those samples as represented in Figure 1b. The UV absorption curves of those samples present two absorption peaks at 255 nm and 347 nm (Figure 2c). The UV spectra (Figure 2d) of CD64 has two weak absorption peaks at 255 nm and 347 nm. The corresponding fluorescence emission spectrum (Figure 2e) of CD64 represents a weak intensity peak at 480 nm as well, suggesting that the coal powder and ethylenediamine contributes to the formation of CDs.

The CDs were formed with the ratio change of ethanol and ethylenediamine, in which the coal powder was the basic materials. The sample represents blue color under daylight and light yellow color under UV-light

(Figure 1a). MCD64 has the strongest fluorescence intensity at 480 nm among those samples as represented in Figure 1b. The UV absorption curves of those samples present two absorption peaks at 255 nm and 347 nm (Figure 2c). The UV spectra (Figure 2d) of CD64 has two weak absorption peaks at 255 nm and 347 nm. The corresponding fluorescence emission spectrum (Figure 2e) of CD64 represents a weak intensity peak at 480 nm as well, suggesting that the coal powder and ethylenediamine contributes to the formation of CDs.

The CDs were formed with the ratio change of ethanol and ethylenediamine, in which the coal powder was the basic materials. The sample represents blue color under daylight and light yellow color under UV-light (Figure 1a). MCD64 has the strongest fluorescence intensity at 480 nm among those samples as represented in Figure 1b. The UV absorption curves of those samples present two absorption peaks at 255 nm and 347 nm (Figure 2c). The UV spectra (Figure 2d) of CD64 has two weak absorption peaks at 255 nm and 347 nm. The corresponding fluorescence emission spectrum (Figure 2e) of CD64 represents a weak intensity peak at 480 nm as well, suggesting that the coal powder and ethylenediamine contributes to the formation of CDs.

The absorption peak of UV absorption at 255 nm (Figure 2a) is derived from the $\pi-\pi^*$ transition of the sp^2 hybrid carbon [13]. The second peak at 347 nm attributes to the $n-\pi^*$ transition of the C=O bond on the surface of MCD64 [14]. The optimal excitation wavelength of MCD64 is 400 nm, which is in good symmetry with the fluorescence emission spectrum (480 nm) at the excitation wavelength of 400 nm. Figure 2b shows that the fluorescence center of MCD64 shifts from 475 nm to

505 nm with the excitation wavelength increasing from 380 nm to 460 nm. The highest response of fluorescence is at 480 nm when excitation wavelength set at 400 nm. Such excitation-dependent fluorescence is related to defects on the surface of the CDs and optimizing the excitation wavelength is necessary [15].

Figure 2c shows that the intensity of MCD64 becomes weak with a blue shift under the acid/alkali environment. The good stability of CDs in NaCl solution relates to the application under complex conditions. The fluorescence emission spectrum measured at $\lambda_{ex} = 400$ nm represents the peak position in consistency, as shown in Figure 2c (inset). The peak intensity of all the curves at different concentration from 0 M to 2.5 M is almost the same. However, at different pH value the fluorescence feature of MCD64 varies obviously (Figure 2d). Around 30 - 35 % decrease is recorded when pH at 1 or 14, suggesting that the surface functional group of CDs might be reacted with proton or hydroxide and weaken the fluorescence [4]. The suitable condition for MCD64 locates in the pH range of 6-9 with a high response of the fluorescence.

The application of the CDs could be applied to discriminate the metal ions in the solution by the variation of fluorescence. The fluorescence intensity of CDs was measured at 400 nm excitation wavelength by adding 5 μ M of Ba^{2+} , Fe^{3+} , Ni^{2+} , Cu^{2+} , Mn^{2+} , Cr^{3+} , Co^{2+} , Zn^{2+} , Mg^{2+} , Na^+ , K^+ solutions to MCD64 solution. Figure 2e clearly shows that only Fe^{3+} has a significant fluorescence quenching effect on the fluorescence intensity of MCD64. The rest metal ions have only a slight effect on the fluorescence intensity. This indicates that MCD64 can specifically recognize Fe^{3+} .

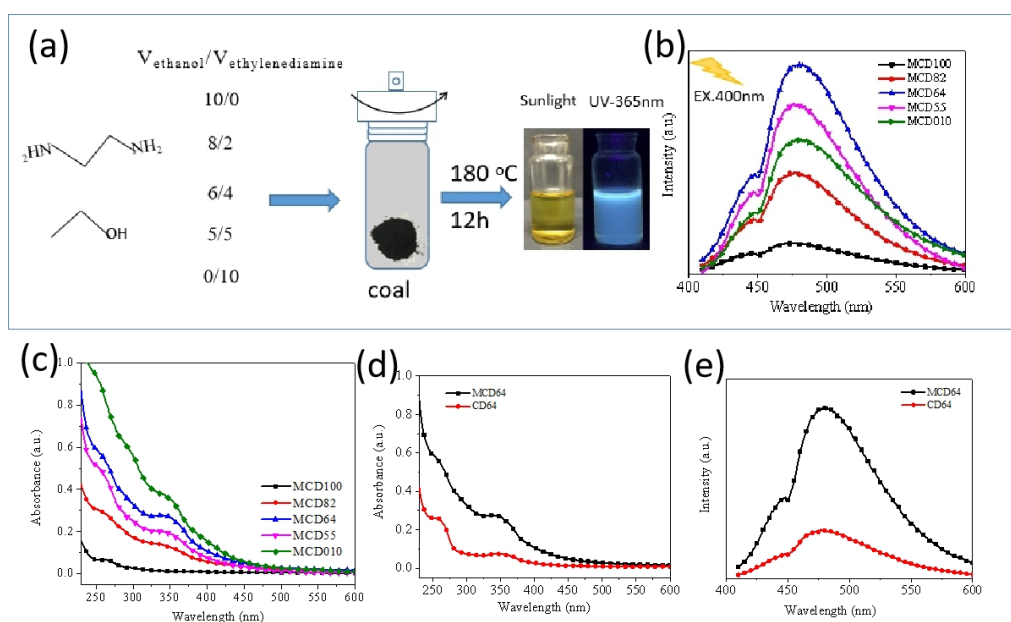


Figure 1 The scheme of synthesis route for CDs with the fluorescence characters (a), the fluorescence emission spectrum at 400 nm excitation wavelength (b), UV absorption curve of coal-based CDs under different systems and (inset) a picture of the sample under 365 nm UV lamp (c), The UV absorption spectra (d) and the fluorescence emission spectrum at an excitation wavelength of 400 nm (e) of the MCD64 and CD64

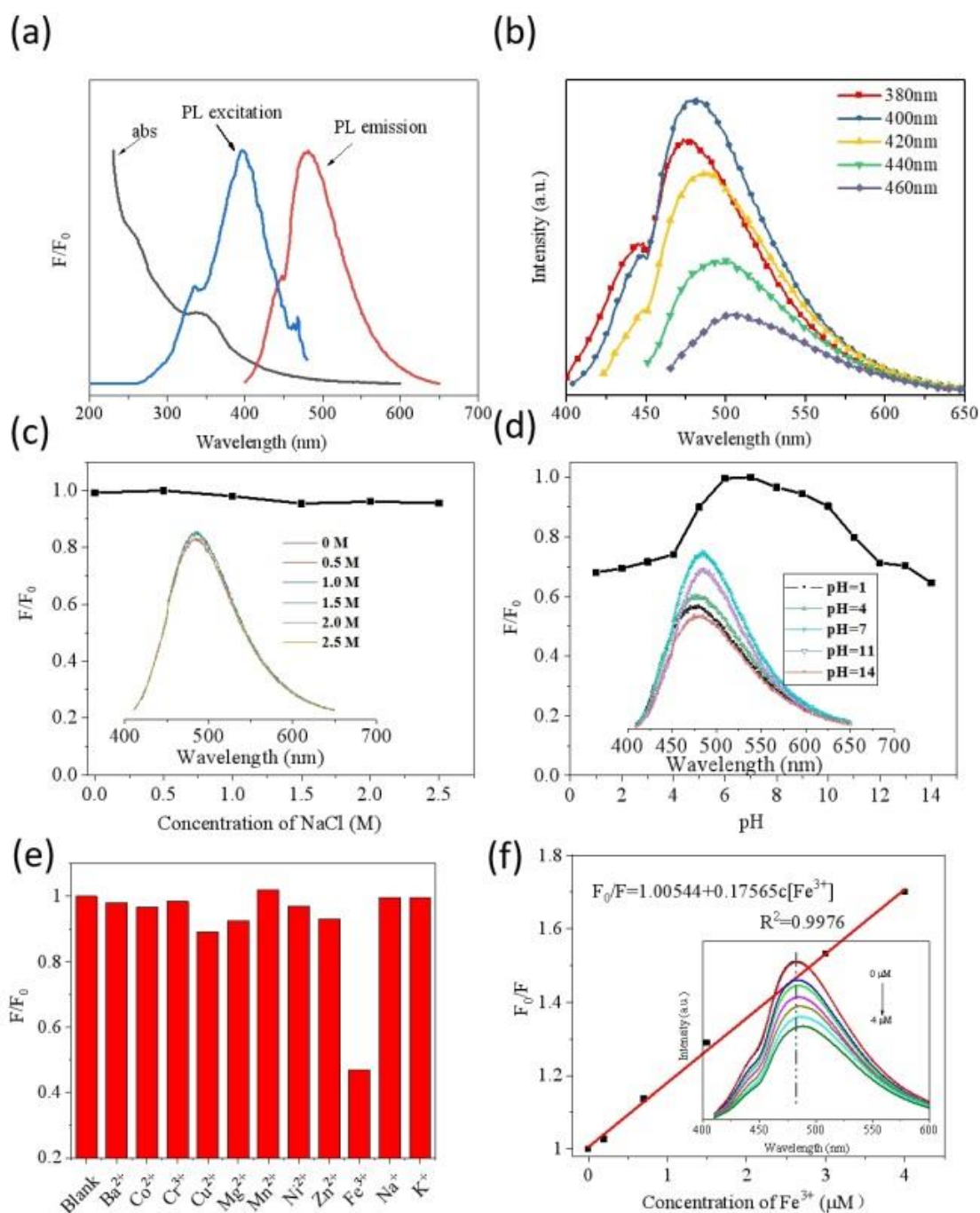


Figure 2 (a) UV-vis spectrum, excitation spectrum and fluorescence emission spectrum of MCD64; (b) Fluorescence emission spectrum of MCD64 at different excitation wavelengths. (c) Effect of NaCl concentration and (inset) The fluorescence curves of CDs in NaCl solution. (d) pH on fluorescence property of CDs and (inset) The fluorescence curves of CDs at different pH solution. (e) Relative PL intensity diagram of MCD64 after adding different kinds of metal ions. (f) Fitting curve for relative PL intensity and (inset) Emission spectrum of MCD64 with Fe^{3+} in the range of 0-4 μM

The specific selection to Fe_{3+} is further evaluated with investigation of the sensitivity. The fluorescence intensity change of the MCD64 and the concentration of Fe_{3+} were linearly fitted based on the Stern-Walmer equation, and the fitting equation was $F_0/F=1.00544+0.17565c[\text{Fe}_{3+}]$ ($R^2=0.9976$), as shown in Figure 2f. As shown in Figure 2f (inset), the fluorescence

intensity of the MCD64 gradually decreases with the Fe_{3+} concentration increases from 0 to 4 μM . The detection limit was calculated according to $3 N/k$ (N is the standard deviation of the fluorescence intensity of the blank sample, k is the slope of the linear fitting equation), and the detection limit is 0.103 μM . The detection limit is better than the detection limit of Fe_{3+} (0.21 μM) of

GCDs, which was obtained by hydrothermal treatment of citric acid and glycine [6]. We believe that the CDs with specific surface states decide the detection limits and detection ranges for Fe₃₊.

3.2 Structural characterization of coal-based CDs

The XRF spectra of coal and MCD-64 revealed the difference between the coal and CDs. Figure 3a shows that the coal has weak peaks at 2.31 keV, 3.69 keV, 4.51 keV and 5.90 keV, corresponding to S, Ca, Ti and Mn elements, respectively. The two peaks at 6.41 keV and 7.11 keV are generated by the α and β emission lines of the Fe element. It is worth noting that the Ar element at 2.96 keV is derived from air. After solvent heat treatment and post-purification treatment the MCD64 represents only the Ar element in the spectra, indicating that no impurities exist in the sample.

The TEM image shows that MCD64 are approximately in spherical shape and dispersed well (Figure 3c). The sizes are all less than 10 nm, mainly concentrated in 2-5 nm, and the average particle size is 3.75 nm (Figure 3c inset). The Figure 3d shows the FT-IR spectra of MCD64 and coal. A significant broad peak at 3435 cm⁻¹ of MCD64 is the characteristic peak

-OH and -NH bonds [17], which is much stronger than that of coal. This indicates that more hydrophilic groups are formed on the surface of MCD64 during the hydrothermal process, and ensure a good water solubility and stability of MCD64 [18]. The absorption peak of the C-H bond located at 3020 cm⁻¹ is observed in MCD64, other than that of the coal, confirming the small sp² hybrid carbon stripped from the coal [19]. The characteristic peaks at 1616 cm⁻¹ and 1409 cm⁻¹ can be attributed to the absorption of the C=O bond and the C=C skeleton [5,20]. 1126 cm⁻¹ is ascribed to the absorption of C-N bond [13], indicating that the N element from ethylenediamine is successfully introduced to the surface of MCD64. The characteristic peak at 1010 cm⁻¹ is attributed to the absorption of the C-OH bond [17], indicating the presence of phenolic hydroxyl groups on the surface of the CDs. Thus MCD64 were successfully prepared based on the existence of the coal powder. Similar to the CDs from citric acid and glycine [6], the surface phenolic hydroxyl groups could react with Fe³⁺ to form a polymer, then the excited state electrons of the CDs transfer to the d-state orbit of Fe³⁺ and the electron-hole pairs recombined, leading to a fluorescence quenching of the CDs.

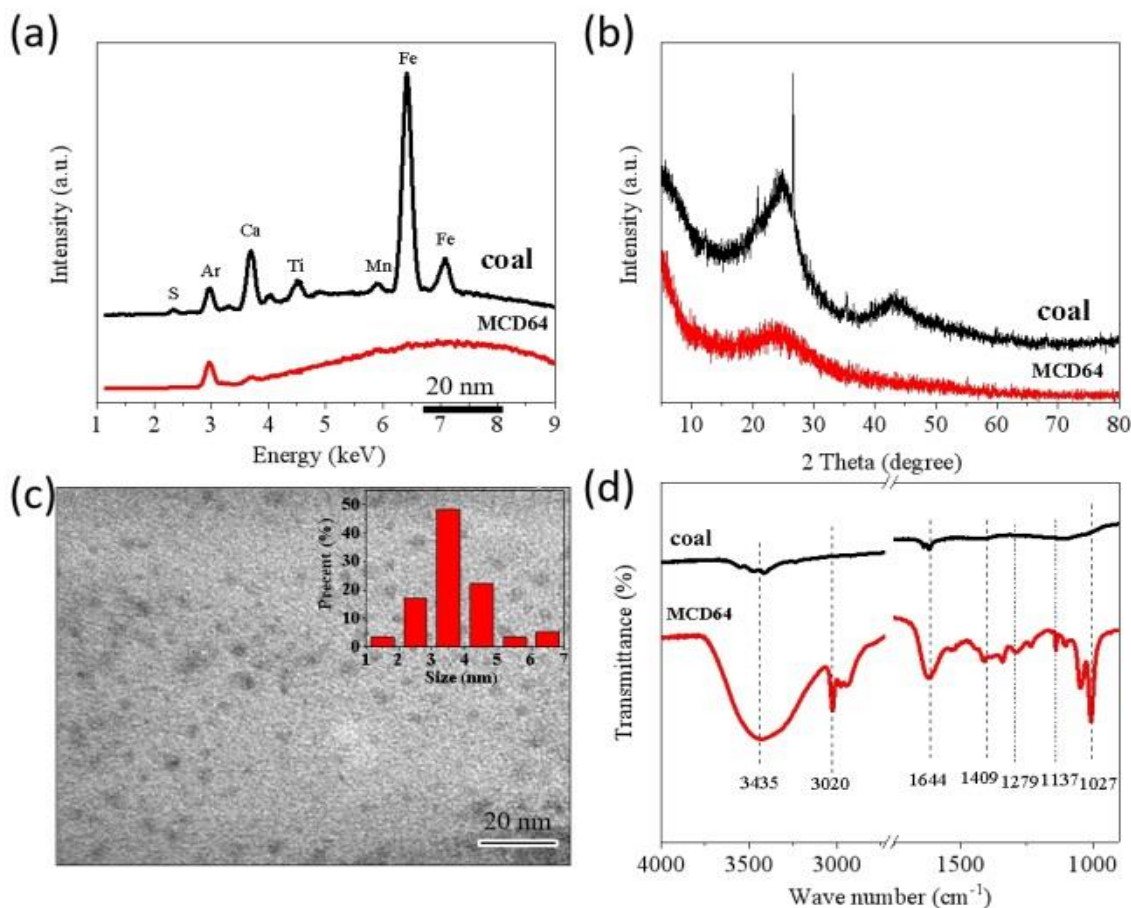


Figure 3 XRF patterns (a) and XRD patterns (b) of coal and MCD64, (c) TEM spectrum and size distribution map of MCD64 (inset) and (d) FTIR spectrum of coal and MCD64 samples

3.3 photoelectric performance analysis of composite photoelectric materials

The CDs could be used as the heteroatoms to improve the photoelectric response of metal oxides [21-24]. Figure 4a shows the energy band curve of the MCD64 modified TiO₂, which is calculated according to the UV-absorption spectrum. The band width of MCD64/TiO₂ is reduced to 2.84 eV from 3.2 eV of TiO₂, suggesting that the doped CDs can effectively accelerate the transition of electrons and generate electron-hole pairs to improve the photoelectric response [25,26].

The fluorescence emission spectroscopy can also be used to characterize the photo-generated charge of photovoltaic materials. The lower fluorescence intensity fits to the less photoelectron recombination efficiency [27]. As shown in Figure 4b, the fluorescence center of the MCD64 sample is at 480 nm at the excitation wavelength of 400 nm, and the emission peak intensity of MCD64/TiO₂ at 480 nm is significantly decreased. The photoelectron recombination efficiency of the composite is reduced, and the presence of coal-based CDs acts to suppress the photoelectron-hole pair recombination of TiO₂,

thereby improving the photoelectric characteristics [24]. Therefore, these results indicate that the prepared coal-based CDs can act as a sensitizer in the composite photovoltaic material, enhance the absorption of visible light and promote the charge transfer efficiency, thereby increasing the possibility of application in photovoltaic materials.

Figure 4c represents that the photoelectric current of TiO₂ is 0.14 $\mu\text{A cm}^{-2}$ under UV light with a light intensity of 10 mW cm^{-2} . After doping MCD64, the photoelectric current is significantly improved to 0.55 $\mu\text{A cm}^{-2}$, which is about 4 times than that of TiO₂. We believe that CDs is irradiated by the ultraviolet lamp, the electron absorption energy transitions to the excited state, and can be quickly transferred to the conduction band of the TiO₂, thereby enhancing the photoelectric response of the composite photoelectric material. The degradation in dark was monitored and the slight increased degradation can be observed (Figure 4d). After the subtraction of the degradation in dark, the degradation rate of MCD64/TiO₂ sample to methylene blue under the UV irradiation for 3.5 hours. A decrease at 75 % was observed with MCD64/TiO₂, which shows a 20 % of augmentation control to the TiO₂ sample.

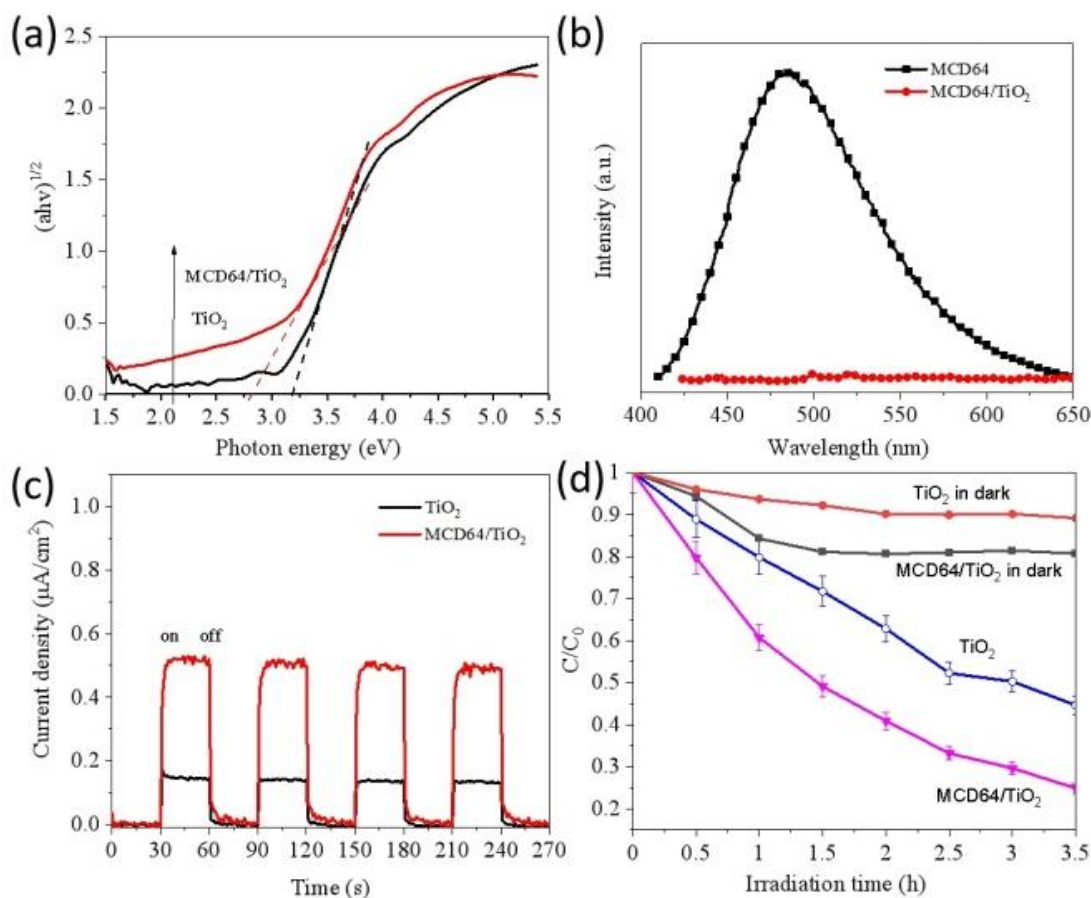


Figure 4 (a) Band gap curve of TiO₂ and MCD64/TiO₂, (b) fluorescence emission spectrum, (c) Photoelectric response of TiO₂ and MCD64/TiO₂, and (d) Methylene blue degradation in dark and UV light

The fluorescence emission spectroscopy can also be used to characterize the photo-generated charge of

photovoltaic materials. The lower fluorescence intensity fits to the less photoelectron recombination efficiency [27].

As shown in Figure 4b, the fluorescence center of the MCD64 sample is at 480 nm at the excitation wavelength of 400 nm, and the emission peak intensity of MCD64/TiO₂ at 480 nm is significantly decreased. The photoelectron recombination efficiency of the composite is reduced, and the presence of coal-based CDs acts to suppress the photoelectron-hole pair recombination of TiO₂, thereby improving the photoelectric characteristics [24]. Therefore, these results indicate that the prepared coal-based CDs can act as a sensitizer in the composite photovoltaic material, enhance the absorption of visible light and promote the charge transfer efficiency, thereby increasing the possibility of application in photovoltaic materials.

Figure 4c represents that the photoelectric current of TiO₂ is 0.14 $\mu\text{A cm}^{-2}$ under UV light with a light intensity

of 10 mW cm^{-2} . After doping MCD64, the photoelectric current is significantly improved to 0.55 $\mu\text{A cm}^{-2}$, which is about 4 times than that of TiO₂. We believe that CDs is irradiated by the ultraviolet lamp, the electron absorption energy transitions to the excited state, and can be quickly transferred to the conduction band of the TiO₂, thereby enhancing the photoelectric response of the composite photoelectric material. The degradation in dark was monitored and the slight increased degradation can be observed (Figure 4d). After the subtraction of the degradation in dark, the degradation rate of MCD64/TiO₂ sample to methylene blue under the UV irradiation for 3.5 hours. A decrease at 75 % was observed with MCD64/TiO₂, which shows a 20 % of augmentation control to the TiO₂ sample.

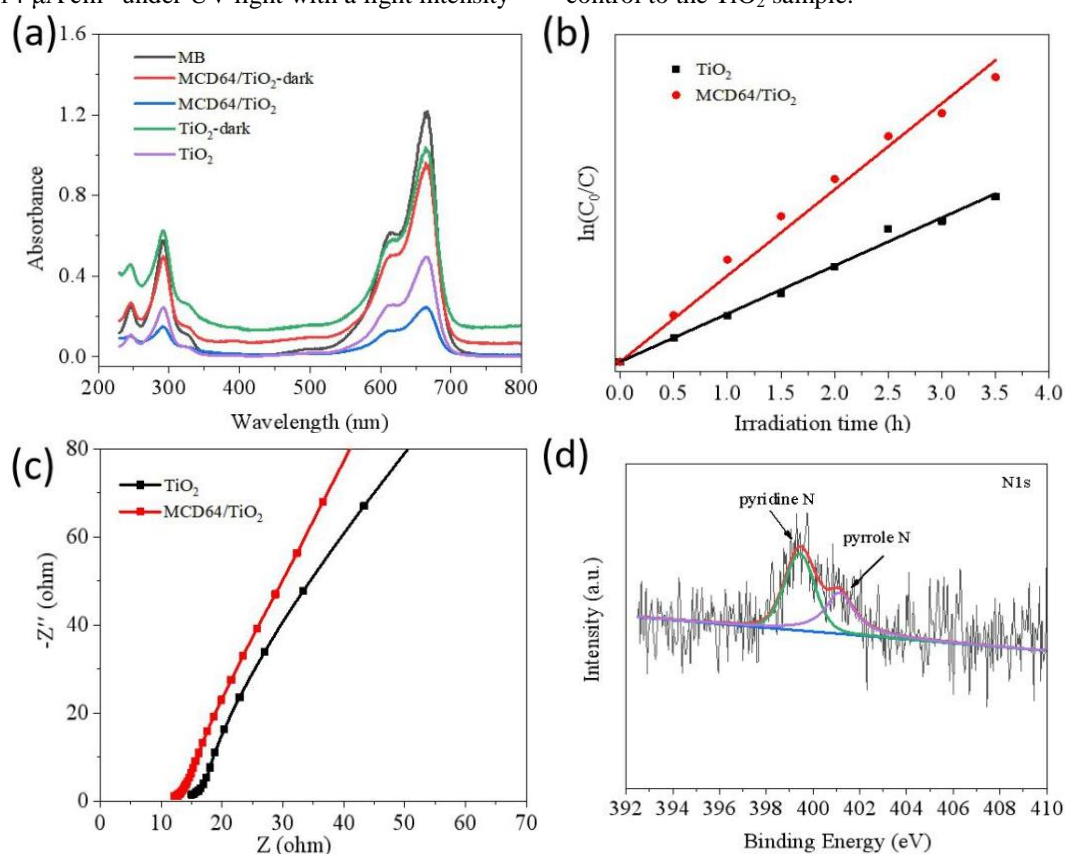


Figure 5 (a) Methylene blue adsorption curve under different condition, (b) the kinetic study equation of of MCD64/TiO₂ and TiO₂ samples, (c) Nyquist plot, (d) XPS survey spectra N1s of MCD64/TiO₂

The photocatalytic degradation characteristics of MCD64/TiO₂ and TiO₂ materials to methylene blue under ultraviolet light were studied. The control experiment was performed with the observation of the absorbance of UV-vis spectra (Figure 5a). The kinetic study of the adsorption data, as shown in Figure 5b, shows a good linear relationship between $\ln(C_0/C)$ and t , which means that the photodegradation process of methylene blue on the photocatalyst follows the rules of first-order reaction kinetics. The apparent reaction rate constant of MCD64/TiO₂ and TiO₂ is 0.42 and 0.23 h^{-1} , respectively, reflecting the promoted photocatalytic degradation process with the coal-made CDs.

The conjugated π structure in the CDs can effectively improve the photocatalytic activity and photoelectric conversion characteristics of the semiconductor material, and can be a new type of photovoltaic material after being chemically combined with TiO₂ [24]. The photocatalytic properties of TiO₂ are derived from electron-hole pairs generated by illumination, the holes generated in the valence band (VB) have strong oxidizing properties and are easy to capture electrons in the solvent, and the photoelectrons on the conduction band (CB) are reducible and undergo oxidation-reduction reaction with organic molecules in the solvent to achieve the purpose of catalysis [22, 23].

Therefore, the combination of TiO₂ with a suitable material suppresses the recombination of the VB electrons and the holes of the CB. An intense redox reaction occurs on the surface of the composite material, enhancing the photocatalytic activity.

The influence of CDs was further confirmed by electrochemical impedance spectroscopy (EIS). The Nyquist plots of MCD64/TiO₂ and TiO₂ are shown in Figure 5c. Since only a single half ring is observed, the equivalent resistance and charge transfer resistance (R_s+R_{ct}) of the electrode material are reflected in the intercept of the high frequency region curve and the real axis [26]. Compared with TiO₂ powder (15 Ω), the composite sample (12 Ω) has smaller equivalent resistance and charge transfer resistance, indicating that the composite optoelectronic material has more efficient charge transfer efficiency. To confirm the effect of ethylenediamine for the formation of MCD64, the XPS survey spectra was investigated. Nitrogen in the sample is 0.97 at%. The high-resolution N1s spectrum possesses two peaks at 399.4 eV and 401.1 eV, ascribing to pyrrole N and pyridine N-oxides [28], respectively. Thus the N element from ethylenediamine is successfully introduced into the CDs (Figure 5d).

The coal is a macromolecular substance formed by the sp² carbon domains through fat chains. During the solvothermal reaction, the high temperature and high pressure environment cause the fatty chain break, and the small debris of carbon nanoparticle from the coal is peeled off with sp² structure [13]. At the same time, the ethylenediamine and ethanol could be split in solvothermal system, thus the functional groups with N atoms improve the fluorescence performance of the CDs [29]. Compared with the strong acid oxidation etching or hydrogen peroxide oxidation preparation process, the solvothermal method easily lead to the formation of CDs with oxygen-containing functional groups. The conjugated structures inhibit non-radioactive recombination of electron-hole pairs [30], resulting in a superior fluorescence performance.

4 Conclusions

We prepared a fluorescent carbon dots with a size of 3.75 nm from coal by one-step solvothermal method. The ethylenediamine was used as both a reaction solvent and a nitrogen-containing precursor in the system. The coal-based CDs showed blue-green fluorescence under ultraviolet light. The coal-based CDs displayed the strongest fluorescence emission at 480 nm under the optimal excitation wavelength of 400 nm, which was sensitive to the Fe³⁺ ions under different circumstance. The coal-based CDs-TiO₂ composite possessed the photoelectric response higher than the TiO₂ four times under the ultraviolet light with intensity of 10 mW cm⁻². It was effective to the photodegradation of methylene blue with a increase of 20 % comparing to the TiO₂. The

coal-based CDs acted as a sensitizer and could effectively enhance the conductive charge transfer rate, which enhanced the photoelectric response of the composite photovoltaic material.

Acknowledgement: This work was supported by the Foundation of State Key Laboratory of High efficiency Utilization of Coal and Green Chemical Engineering, Ning Xia University (2020-KF-22), Special project of Science and Technology Department, Xinjiang Uygur Autonomous Region (2020D03025) and the Natural Science Foundation of Xinjiang Uygur Autonomous Region (2021D01A03).

References

- [1] Hu S, Wei Z, Chang Q, et al. Facile and green method towards coal-based fluorescent carbon dots with photocatalytic activity. *Applied Surface Science* 2016, 378: 402-407.
- [2] Namdari P, Negahdari B, Eatemadi A. Synthesis, properties and biomedical applications of carbon-based quantum dots: An updated review. *Biomedicine & pharmacotherapy*, 2017, 87: 209-222.
- [3] Molaei M J, A review on nanostructured carbon quantum dots and their applications in biotechnology, sensors, and chemiluminescence. *Talanta* 2019, 196: 456-478.
- [4] Sun C, Zhang Y, Wang P, et al. Synthesis of Nitrogen and Sulfur Co-doped Carbon Dots from Garlic for Selective Detection of Fe³⁺. *Nanoscale research letters* 2016, 11(1): 110.
- [5] Liu S, Liu R, Xing X, et al. Highly photoluminescent nitrogen-rich carbon dots from melamine and citric acid for the selective detection of iron(III) ion. *Rsc Advances* 2016, 6(38): 31884.
- [6] Feng R Q, Yuan Z Y, Ren T Z. A facile hydrothermal method for preparation of fluorescent carbon dots on application of Fe³⁺ and fingerprint detection. *Methods and applications in fluorescence* 2019, 7(3): 35001.
- [7] Yu H, Zhao Y, Zhou C, et al. Carbon quantum dots/TiO₂ composites for efficient photocatalytic hydrogen evolution. *Journal of Materials Chemistry A* 2014, 2(10): 3344-3351.
- [8] Zhang B, Halidan M, Zhang D, et al. Preparation of coal-based C-Dots/TiO₂ and its visible-light photocatalytic characteristics for degradation of pulping black liquor. *Journal of Photochemistry and Photobiology a-Chemistry* 2017, 345: 54-62.
- [9] Hoang, V. C, Hassan, M, Gomes, V. G., Coal derived carbon nanomaterials – Recent advances in synthesis and applications. *Applied Materials Today* 2018, 12, 342-358.
- [10] Hu C, Yu C, Li M, et al. Chemically tailoring coal to fluorescent carbon dots with tuned size and their capacity for Cu (II) detection. *Small* 2014, 10(23): 4926-4933.
- [11] Geng B, Yang D, Zheng F, et al. Facile conversion of coal tar to orange fluorescent carbon quantum dots and their composite encapsulated by liposomes for bioimaging. *New Journal of Chemistry* 2017, 41 (23): 14444-14451.

- [12] Zhang B, Halidan M, Zhang Y F, et al. Preparation of Coal-based C-dots and Their Application in Trace Cu(II) Detection. *Chinese Journal of Analytical Chemistry* 2017, 45 (10): 1489-1496.
- [13] Li M, Hu C, Yu C, et al. Organic amine-grafted carbon quantum dots with tailored surface and enhanced photoluminescence properties. *Carbon* 2015, 91: 291-297.
- [14] Li M, Yu C, Hu C, et al. Solvothermal conversion of coal into nitrogen-doped carbon dots with singlet oxygen generation and high quantum yield. *Chemical Engineering Journal* 2017, 320: 570-575.
- [15] Liu Q, Zhang J, He H, et al. Green Preparation of High Yield Fluorescent Graphene Quantum Dots from Coal-Tar-Pitch by Mild Oxidation. *Nanomaterials* 2018, 8 (10): 844.
- [16] Thiyagarajan S K, Raghupathy S, Palanivel D, et al. Fluorescent carbon nano dots from lignite: unveiling the impeccable evidence for quantum confinement. *Physical Chemistry Chemical Physics* 2016, 18 (17): 12065-12073.
- [17] Gu D, Shang S, Yu Q, et al. Green synthesis of nitrogen-doped carbon dots from lotus root for Hg(II) ions detection and cell imaging. *Applied Surface Science* 2016, 390: 38-42.
- [18] Singamaneni S R, Van T J, Ye R, et al. Intrinsic and extrinsic defects in a family of coal-derived graphene quantum dots. *Applied Physics Letters* 2015, 107: 212402.
- [19] Li H, Guo X, Liu J, et al. A synthesis of fluorescent starch based on carbon nanoparticles for fingerprints detection. *Optical Materials* 2016, 60: 404-410.
- [20] Dutta Chowdhury A, Doong R A. Highly Sensitive and Selective Detection of Nanomolar Ferric Ions Using Dopamine Functionalized Graphene Quantum Dots. *ACS applied materials & interfaces* 2016, 8 (32): 21002-10.
- [21] Zhuo S, Shao M, Lee S T. Upconversion and Downconversion Fluorescent Graphene Quantum Dots: Ultrasonic Preparation and Photocatalysis. *Acs Nano* 2012, 6(2): 1059-1064.
- [22] Li Y, Xia Y, Liu K, et al. Constructing Fe-MOF-Derived Z-Scheme Photocatalysts with Enhanced Charge Transport: Nanointerface and Carbon Sheath Synergistic Effect [J]. *ACS Applied Materials & Interfaces*, 2020, 12: 25494–25502.
- [23] Huang Y, Guo Z, Liu H, et al. Heterojunction Architecture of N - Doped WO₃ Nanobundles with Ce₂S₃ Nanodots Hybridized on a Carbon Textile Enables a Highly Efficient Flexible Photocatalyst[J]. *Advanced Functional Materials*, 2019, 29(45), 1903490.
- [24]. Zhou J, Chen J, Zheng J, et al. Role of carbon quantum dots in titania based photoelectrodes: Upconversion or others? *Journal of colloid and interface science* 2018, 529: 396-403.
- [25] Zhang Y, Zeng W, Ye H, et al. Enhanced carbon monoxide sensing properties of TiO₂ with exposed (001) facet: A combined first-principle and experimental study. *Applied Surface Science* 2018, 442: 507-516.
- [26] Babar P T, Lokhande A C, Pawar B S, et al. Electrocatalytic performance evaluation of cobalt hydroxide and cobalt oxide thin films for oxygen evolution reaction. *Applied Surface Science* 2018, 427: 253-259.
- [27] Cheng C, Lu D, Shen B, et al. Mesoporous silica-based carbon dot/TiO₂ photocatalyst for efficient organic pollutant degradation. *Microporous and Mesoporous Materials* 2016, 226: 79-87.
- [28] Xu S, Qiu S, Yuan Z, et al. Nitrogen-containing activated carbon of improved electrochemical performance derived from cotton stalks using indirect chemical activation[J]. *Journal of Colloid And Interface Science*, 2019, 540: 285-294.
- [29] Zhai X, Zhang P, Liu C, Bai, et al. Highly luminescent carbon nanodots by microwave-assisted pyrolysis. *Chemical communications* 2012, 48 (64): 7955-7.
- [30] Ming H, Ma Z, Liu Y, et al. Large scale electrochemical synthesis of high quality carbon nanodots and their photocatalytic property. *Dalton Transactions* 2012, 41(31): 9526-9531.

Monodisperse SiO₂ Microspheres with Large Specific Surface Area: Preparation and Particle Size Control

Shengkai LI¹, Xianjin XU², Wei LI¹, Lei WANG^{1*}, Haijin NING^{2*}, Shengliang ZHONG^{1*}

1. Research Center for Ultrafine Powder Materials, College of Chemistry and Chemical Engineering, Jiangxi Normal University, Nanchang 330022, China

2. Jiangxi KingPowder New Material Co., Ltd., Ganzhou 341003, China

*Corresponding authors: Lei WANG, Haijin NING, E-mail: slzhong@jxnu.edu.cn (S. L. Zhong)

Abstract:

Monodisperse SiO₂ microspheres have found applications in catalysis, drug delivery, coatings, cosmetics, optical sensing and plastics. The particle size of monodisperse SiO₂ microspheres is closely related to its application. In this paper, monodisperse SiO₂ microspheres with tunable diameter were successfully synthesized using cetyltrimethylammonium bromide (CTAB) as template. The monodisperse SiO₂ microspheres with diameters ranging from 200 nm to 3 μm were obtained by controlling the concentration of CTAB, tetraethyl orthosilicate (TEOS), diethanolamine (DEA) and reaction temperature. The BET surface area could reach 835 m² g⁻¹ and mean pore diameter was 2.3 nm. The formation mechanism of monodisperse SiO₂ microspheres was investigated.

Keywords: Monodisperse; SiO₂ microspheres; template method

1 Introduction

For the past few years, the superior performance of nanomaterials has received extensive attention from scholars. Monodisperse mesoporous SiO₂ microspheres have been widely used in catalysis^[1-5], drug loading^[6-8], coatings^[9-10], optical sensing^[11], plastics and other fields by virtue of their large specific surface area, good biocompatibility, stable physical and chemical properties, and easy functionalization of surface hydroxyl groups^[12].

As we all know, the particle size of monodisperse SiO₂ microspheres plays a decisive role in their application. For example, nanoscale monodisperse SiO₂ microspheres are widely used in biopharmaceuticals^[13], and micron-sized monodisperse SiO₂ microspheres are mostly used in cosmetics, coatings and other fields^[14-17]. Sol-gel method is the most widely used method for preparing SiO₂ particles^[18]. However, the size of SiO₂ spheres is less than 900 nm and can only be regulated between 10-500 nm. Although seed-mediated growth method can be used to prepare SiO₂ microspheres with a wider range of particle size, this reaction requires strict control of the proportion of various raw materials, as well as the addition rate of tetraethyl orthosilicate, stirring rate, reaction time, and other factors. The preparation of SiO₂ microspheres by a multi-step synthesis method is complicated and time-consuming. It

is easy to cause agglomeration or multiple nucleation during the growth of particles. Lei and his team used a modified sol-gel method to synthesize SiO₂ microspheres with particle sizes ranging from 1 μm to 3 μm^[19]. Monodisperse SiO₂ was prepared by a two-phase reaction. The monodisperse SiO₂ microspheres with core-shell structure were obtained by controlling the stirring speed, and specific surface area reached 233 m² g⁻¹^[20]. To extend the application of monodisperse SiO₂ microspheres in different fields, it is still a great challenge to prepare monodisperse SiO₂ microspheres with a wide particle size range and large specific surface area.

In this work, using cetyltrimethylammonium bromide (CTAB) as a template and diethanolamine (DEA) as a catalyst, monodisperse SiO₂ microspheres with particle sizes ranging from 200 nm to 3 μm were successfully synthesized and the effects of different reaction conditions to the morphology of the prepared monodisperse SiO₂ microspheres were studied and discussed.

2 Experimental section

2.1 Materials

DEA (99 %) and ethanol (99 %) were purchased from Damao Chemical Reagent Company (Tianjin, China). tetraethyl orthosilicate (TEOS, analytical grade) and CTAB (99 %) were obtained from

Aladdin Reagent Company (Shanghai, China). Deionized water was used in all experiments. All chemicals were used as received without purification.

2.2 Preparation of monodisperse SiO₂ microspheres

In a typical experiment, 0.08 g CTAB was dissolved in 15 mL water under stirring in a beaker. The obtained clear solution was heated to 30 °C in water bath. 15.0 mL TEOS (0.1 mol/L) was dropped into the above solution under stirring. And then, 2.0 mL DEA (0.1 mol/L) was slowly dropped into the above mixture under stirring. After stirring for 30 minutes, the mixture was kept under static conditions for 24 hours. The resulting monodisperse SiO₂ microspheres (sample 1) were separated by centrifuging and washed with ethanol twice and distilled water once and then dried in an oven at 60 °C. In order to eliminate the organic residues, the obtained products were thermal treated at 550 °C for 2 h in the air.

2.3 Characterization

The morphologies of the products were observed by a SEM equipped with an EDS (Hitachi, S-3400N). The nitrogen adsorption and desorption isotherms were measured on a BELSORP-mini II apparatus. The pore size and the pore diameter distributions were derived from the desorption branches of the isotherm with the Barrett-Joyner-Halenda (BJH) model. X-ray diffraction (XRD) patterns were collected using a Rigaku/Max-3A X-ray diffractometer with Cu-K α radiation ($\lambda = 1.54178$ Å) at a voltage of 30 kV and a current of 10 mA. ATA-50 thermal analyzer was used to record the TG curve at a

heating rate of 10 °C min⁻¹ from room temperature to 800 °C under an air atmosphere.

3 Results and discussion

3.1 Characterization of the typical product

SEM was carried out to observe the size and morphology of the synthesized sample 1. Figure 1 shows that the sample is composed of a large number of spheres with smooth surface and uniform particle size. Figure 2 is the energy spectrum of the sample. In order to further analyze the sample composition, XRD pattern of sample 1 is shown in Figure 3. The diffraction peak centered at 22° indicates that the obtained sample is amorphous structure SiO₂^[21]. Figure 4 shows the thermogravimetric spectrum of the prepared sample. It can be seen from the thermogravimetric curve of the sample that the first weight loss is between 40 and 200 °C, mainly due to the desorption process of water molecules adsorbed on the surface of the silica microspheres. The second weight loss is between 200 and 550 °C, presumably caused by the decomposition of surfactants and some organic substances in the sample, and the two weight loss rates are about 25%. Figure 5 shows a type I isotherm implying the existence of mesoporous, which is confirmed by the pore diameter distribution curve. Sample 1 has a specific surface area of 835 m² g⁻¹ and the mean pore diameter is 2.3 nm. From the above characterization, it can be seen that Sample 1 is a monodisperse silica microsphere with high purity and amorphous structure.

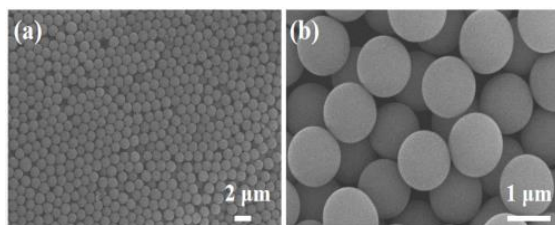


Figure 1 SEM images of sample 1

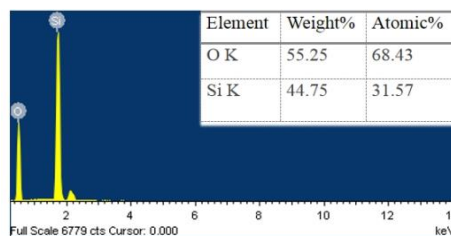


Figure 2 EDX spectrum of sample 1

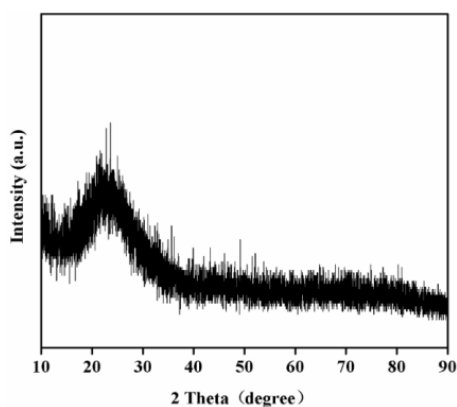


Figure 3 PXRD patterns of sample 1

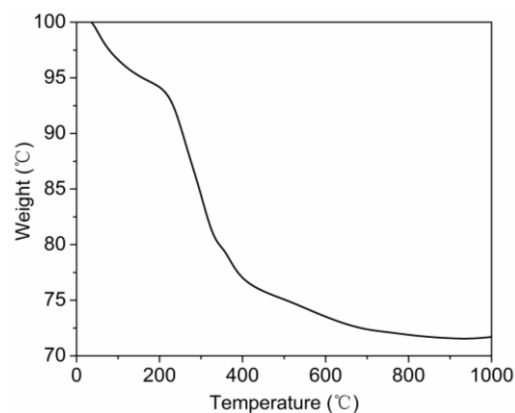


Figure 4 TG curve of the silica microspheres

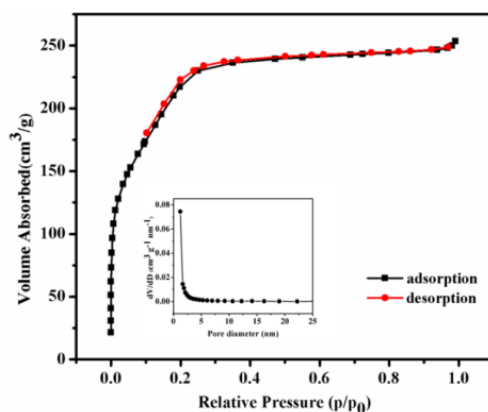


Figure 5 Nitrogen adsorption-desorption isotherms of sample 1 and the corresponding BJH pore size distribution curves

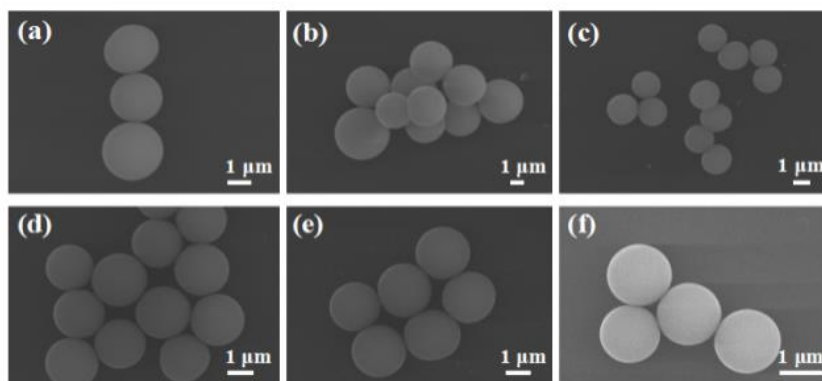


Figure 6 SEM images of SiO₂ particles obtained with different amount of CTAB in the solution: (a) 0.01 g, (b) 0.02 g, (c) 0.03 g, (d) 0.05 g, (e) 0.06 g, (f) 0.08 g

3.2 Effect of the CTAB on particle size and morphology

In the absence of CTAB as a template, no precipitation was observed in the solution, because the TEOS cannot undergo hydrolytic polycondensation. When the concentration of CTAB is low, the size of SiO₂ microspheres is uneven and the sphericity is not good, because low concentration of CTAB leads to the formation of very large micelles which is called worm-like micelles. When the concentration is greater than the critical micelle concentration, the shape of the

micelles is usually spherical [22-23]. In a typical experiment, at the same concentration of TEOS, the particle size of the monodisperse SiO₂ microspheres gradually decreases from 2.28 μm to 1.53 μm with the increase of CTAB (Figure 6), the particle size of the monodisperse SiO₂ microspheres gradually decreases to the similar size. Finally, the size of the SiO₂ microspheres was uniform and spherical. Figure 7 shows the size of the monodisperse SiO₂ microspheres, the corresponding particle sizes are 2.28, 2.05, 1.70, 1.80, 1.70, 1.53 μm.

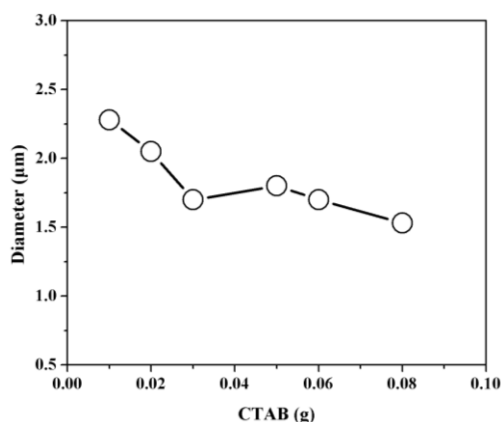


Figure 7 Effect of the amount of CTAB in the solution on the particle diameter

3.3 Effect of DEA on particle size

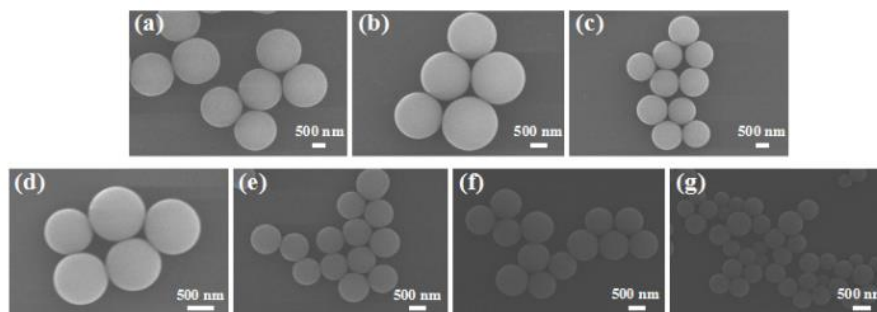


Figure 8 SEM images of SiO₂ particles obtained with different amount of DEA in the solution: (a) 1 mL, (b) 2 mL, (c) 3 mL, (d) 4 mL, (e) 5 mL, (f) 7 mL, (g) 9 mL

It can be seen from the Figure 8 that the particle size of the monodisperse SiO₂ microspheres gradually decreases from 1.70 μm to 0.55 μm with the increase of DEA. This is thought to be caused by the increasing of the hydrolysis rate of TEOS with the increase of DEA concentration, and thus resulting in the formation of SiO₂ core particles are formed in the early stage. At the same time, the DEA has the dual nature of ammonia and

alcohol and it partially ionizes in water, which effectively controls the alkaline environment of the system. The hydroxyl group in the molecule of DEA can also be complexed with the silicon hydroxyl group to terminate the self-condensation of the TEOS [24]. Figure 9 shows the size of monodisperse SiO₂ microspheres, the corresponding particle size is 1.70, 1.53, 1.16, 1.03, 0.82, 0.76, 0.55 μm , respectively.

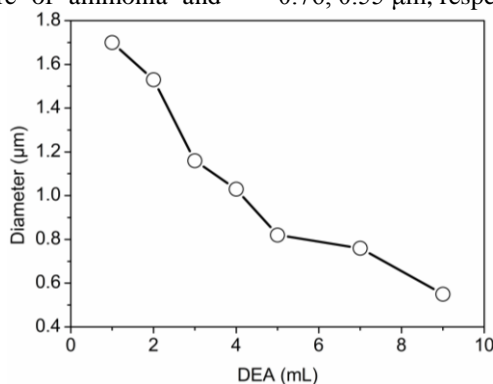


Figure 9 Effect of the DEA on the particle diameter

3.4 Effect of the TEOS on the particle size

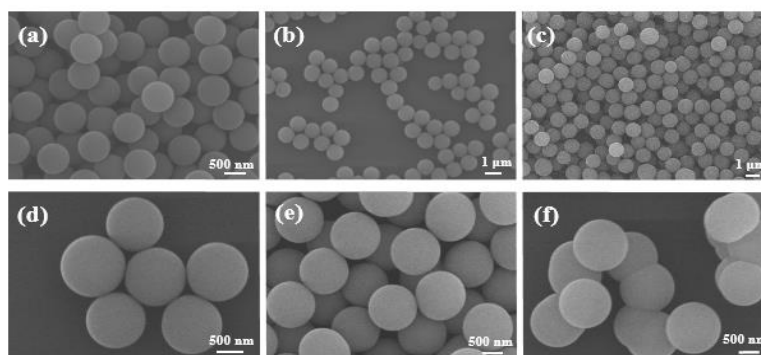


Figure 10 SEM images of SiO₂ particles obtained with different amount of TEOS in the solution: (a) 0.01 mol/L, (b) 0.05 mol/L, (c) 0.1 mol/L, (d) 0.15 mol/L, (e) 0.2 mol/L, (f) 0.3 mol/L

It can be seen from the Figure 10 that the particle size of the monodisperse SiO₂ microspheres increases gradually from 0.75 μm to 1.34 μm with the increase of the concentration of

TEOS. However, too high concentration of TEOS destabilizes the reaction system, leading to the adhesion of SiO₂ microspheres [25-26]. The conclusion is that with the

increase of TEOS, the particle size of SiO₂ microspheres increases and the output is improved. Figure 11 shows the

size of monodisperse SiO₂ microspheres, the corresponding particle size is 0.75, 1.07, 1.13, 1.16, 1.18, 1.34 μm.

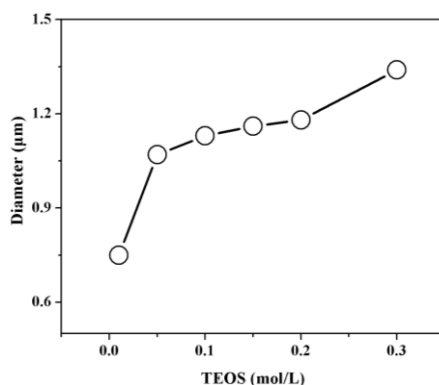


Figure 11 Effect of the TEOS on the particle diameter

3.5 Effect of temperature on the particle size

Experiments were carried out at different temperatures to investigate the effect of temperature on the formation of SiO₂ spheres. It was found that the reaction at low temperature was slow under the condition of equal DEA. With the increase of temperature, precipitation time is shortened, and precipitation occurs immediately at 60 °C. It can be seen from the Figure 12 that the particle size of the monodisperse SiO₂ microspheres decreases with the increase of temperature. At the same concentration of

TEOS, due to the slow hydrolysis rate of TEOS at low temperature, the formation of small particles of silicic acid nuclei is less, and the main reaction is polycondensation, which leads to the growth of SiO₂ microspheres. When the temperature is high, the hydrolysis rate of TEOS is accelerated. In the early stage, a large amount of TEOS is consumed to form a large number of small nucleating particles. In the later stage, smaller microspheres are formed [27]. As shown in Figure 13, the corresponding particle size is 1.53, 1.25, 1.13, 0.91, 0.87, 0.25 μm.

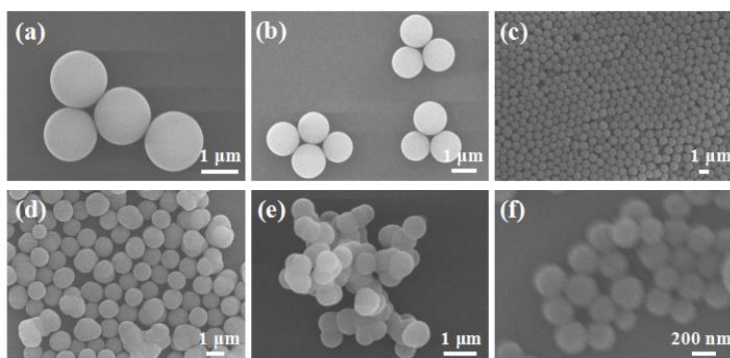


Figure 12 SEM images of SiO₂ particles obtained at different temperatures: (a) 5 °C, (b) 20 °C, (c) 30 °C, (d) 40 °C, (e) 50 °C, (f) 60 °C

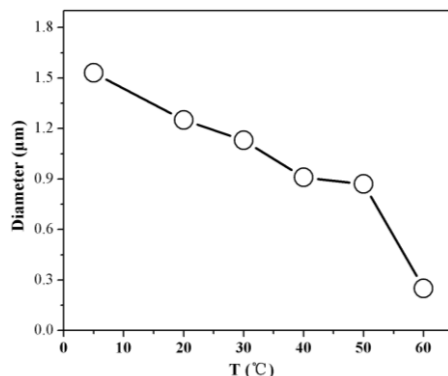


Figure 13 Effect of temperature on the particle diameter

4 Conclusions

Monodisperse SiO₂ microspheres with diameter from 200 nm to 3 μm are synthesized successfully by a template method, and BET surface area could reach 835 m² g⁻¹, mean pore diameter was 2.3 nm. The particle size range of the preparation of monodisperse SiO₂ microspheres was expanded, with the increase of CTAB concentration, the role of template causes SiO₂ microspheres to change from non-spherical to spherical and particle size of SiO₂ microspheres gradually decreased and remained unchanged. The sphericity and dispersion of SiO₂ microspheres gradually increased. With increase of DEA or temperature, the hydrolysis rate of TEOS is increased, more silicic acid nucleus particles are formed in the early stage, leading to the formation of smaller SiO₂ microspheres. The modest increase of TEOS concentration contributes to SiO₂ microspheres growth.

Acknowledgements: This work was supported by Jiangxi Provincial Department of Science and Technology (Nos. 20192BBEL50017 and 20202ACBL203002), the National Natural Science Foundation of China (No. 91622105).

References

- [1] K M Mantovani, K C Molgero Westrup, D S J Rm, et al. Oxidation catalyst obtained by the immobilization of layered double hydroxide/Mn (iii) porphyrin on monodispersed silica spheres. *Dalton Transactions*, 2018, 47: 3068-3073.
- [2] S Cao, J Chang, L Fang, et al., Metal nanoparticles confined in the nanospace of double-shelled hollow silica spheres for highly efficient and selective catalysis. *Chemistry of Materials*, 2016, 28: 5596-5600.
- [3] A Fong, Y Yuan, S L Ivry. Computational kinetic discrimination of ethylene polymerization mechanisms for the Phillips (Cr/SiO₂) catalyst. *ACS Catalysis*, 2015, 5: 3360-3374.
- [4] S L Zhong, L F Zhang, A W Xu. Entropically driven formation of ultralong helical mesostructured organosilica nanofibers. *Small*, 2014, 10: 888-894.
- [5] H C Wu, J H Wu, et al., Influence of sodium-modified Ni/SiO₂ catalysts on the tunable selectivity of CO₂ hydrogenation: Effect of the CH₄ selectivity, reaction pathway and mechanism on the catalytic reaction. *Journal of Colloid and Interface Science*, 2021, 586: 514-527.
- [6] E Bagheri, L Ansari, K Abnous, et al. Silica based hybrid materials for drug delivery and bioimaging. *Journal of Controlled Release*, 2018, 277: 57-76.
- [7] Z Xu, X Ma, Y E Gao, et al. Multifunctional silica nanoparticles as a promising theranostic platform for biomedical applications. *Materials chemistry frontiers*, 2017, 1: 1257-1272.
- [8] J Zhou, F Zhu, J Li, et al. Concealed body mesoporous silica nanoparticles for orally delivering indometacin with chiral recognition function. *Materials Science and Engineering: C*, 2018, 90: 314-324.
- [9] P V Naik, L H Wee, M Meledina, et al. PDMS membranes containing ZIF-coated mesoporous silica spheres for efficient ethanol recovery via pervaporation. *Journal of Materials Chemistry A*, 2016, 4: 12790-12798.
- [10] L. K. Wu, J. J. Wu, W. Y. Wu, et al., Hot corrosion behavior of electrodeposited SiO₂ coating on TiAl alloy. *Corrosion Science* 174, 108827 (2020).
- [11] X Lu, G B Zhou, J Zhang, et al. Highly Sensitive Determination of 2,4,6-Trichlorophenol by Using a Novel SiO₂@MIPIL Fluorescence Sensor with a Double Recognition Functional Monomer. *ACS sensors*, 2020, 5: 1445-1454.
- [12] K Puchnin, V Grudtsov, M Andrianova, et al. A Surface Modifier for the Production of Selectively Activated Amino Surface Groups. *Coatings*, 2019, 9: 726-740.
- [13] P Formoso, R Muzzalupo, L Tavano, et al. Nanotechnology for the environment and medicine. *Mini reviews in medicinal chemistry*, 2016, 16, 668-675.
- [14] S Huang, Z Li, L Kong, et al., Enhancing the stability of CH₃NH₃PbBr₃ quantum dots by embedding in silica spheres derived from tetramethyl orthosilicate in "waterless" toluene. *Journal of the American Chemical Society*, 2016, 138, 5749-5752.
- [15] Z Iqbal, Azhar E, E N Maraj. Performance of nano-powders SiO₂ and SiC in the flow of engine oil over a rotating disk influenced by thermal jump conditions. *Physica A: Statistical Mechanics and its Applications*, 2021, 565, 125570-125584.
- [16] L R Rowe, B S Chapman, J B Tracy, et al. Understanding and controlling the morphology of silica shells on gold nanorods. *Chemistry of Materials*, 2018, 30, 6249-6258.
- [17] B S Chapman, W C Wu, J B Tracy, et al. Heteroaggregation approach for depositing magnetite nanoparticles onto Silica-overcoated gold nanorods. *Chemistry of Materials*, 2017, 29, 10362-10368.
- [18] P Cheng, M Zheng, Y Jin, et al. Preparation and characterization of silica-doped titania photocatalyst through sol-gel method. *Materials Letters*, 2003, 57, 2989-2994.
- [19] X Lei, B Yu, H L Cong, et al. Synthesis of monodisperse silica microspheres by a modified stöber method. *Integrated Ferroelectrics*, 2014, 154, 142-146.
- [20] Q Qu, Y Min, L Zhang, et al. Silica microspheres with fibrous shells: synthesis and application in HPLC. *Analytical chemistry*, 2015, 87: 9631-9638.
- [21] H Hadoun, Z Sadaoui, N Souami, et al. Characterization of mesoporous carbon prepared from date stems by H₃PO₄ chemical activation. *Applied Surface Science*, 2013, 280: 1-7.
- [22] H Gao, Y Zhou, X Sheng, et al. Synthesis of core-shell and hollow structured dual-mesoporous silica templated by alkoxysilyl-functionalized ionic liquids and CTAB. *Materials*

- Letters, 2018, 211: 126-129.
- [23] B Peng, Y X Zong, M Z Nie, et al. Interfacial charge shielding directs the synthesis of dendritic mesoporous silica nanospheres by a dual-templating approach. *New Journal of Chemistry*, 2019, 43: 15777-15784.
- [24] Z A Qiao, L Zhang, M Guo, et al. Synthesis of mesoporous silica nanoparticles via controlled hydrolysis and condensation of silicon alkoxide. *Chemistry of Materials*, 2009, 21: 3823-3829.
- [25] X Luo, J Dong, L Zhang, et al., Preparation of silica microspheres via a semibatch sol-gel method. *Journal of Sol-Gel Science and Technology*, 2017, 81: 669-677.
- [26] Q T Pham, Z H Yao, Y T Wang, et al. Preparation and characterization of monodisperse silica nanoparticles via miniemulsion sol-gel reaction of tetraethyl orthosilicate. *Journal of Materials Science*, 2017, 52, 12706-12716.
- [27] M Meier, J Ungerer, M Klinge, et al. Synthesis of nanometric silica particles via a modified Stöber synthesis route. *Colloids and Surfaces A: Physicochemical and Engineering Aspects*, 2018 538, 559-564.

B, N-Co-doped Carbon Tubes with P Encapsulated in 3D Graphene Aerogel for High-stable Lithium-ion Batteries

Fengfeng XU*, Jian LIN*, Cuiyan TONG*, Haizhu SUN*

National & Local United Engineering Laboratory for Power Battery, College of Chemistry, Northeast Normal University, Changchun 130024, China

*Corresponding Author: Haizhu SUN, E-mail: sunhz335@nenu.edu.cn, Feng-Feng XU and Jian LIN contributed equally to this work.

Abstract:

Li-related anodes with stable ability and excellent rate performance are urgently being pursued to overcome the slow kinetic of current lithium ion storage devices. In this work, an annealing-hydrothermal method is developed to fabricate the anode of a three-dimension nano-construction with robust charge transfer networks, which is composed of elements B, N co-doped carbon tube (BN-CT) as the carrier of red phosphorous to (3D BN-CT@P). Then, 3D BN-CT@P is embedded in the graphene aerogel network to obtain 3D BN-CT@P@GA. Impressively, the 3D BN-CT@P@GA shows high capacity and good cycle stability in the potential range of 0.01-2.5V. Especially, the discharge capacity is $\sim 800 \text{ mAh g}^{-1}$ at 500 mA g^{-1} after 500 cycles when evaluated as anode materials for lithium-ion batteries (LIBs). The improved electrochemical performances result from the unique structure of the 3D BN-CT@P@GA. With the hetero atoms doping, the active P can load up to the BN-CT, which can realize the high capacity as well as the low potential for the anode. At the same time, the graphene aerogel network provides the protection for the BN-CT@P species and good conductivity to enhance ion diffusion. This work fundamentally presents an effective structural engineering way for improving the performance of P-based anodes for advanced LIBs.

Keywords: red phosphorus; nanostructure; anode material; lithium-ion batteries

1 Introduction

Environmental issues and the rapid development of electronic products make it urgent to improve the performance of energy storage devices. As one of the most promising energy storage devices, lithium-ion battery (LIBs) has attracted lots of interests because of their low cost and high energy density^[1-3]. Graphite possesses a theoretical capacity of 372 mAh g^{-1} which is used for commercial LIB anode materials^[4]. However, the higher capacity is indispensable for the high energy storage system. For anode electrodes, higher theory capacity and the lower potential are two important factors for the high energy density. In addition, it is worth noting that the lower potential in anode will involve in the safety hazard because the approach of Li-formation potential (0 V). Therefore, it is significant to develop novel kind of anode materials.

Red phosphorus (P) has aroused extensive attention in LIBs due to its high theoretical specific capacity of 2596 mAh g^{-1} ^[5-6]. Moreover, red phosphorus shows the relatively low and safe working potential ($\sim 0.7 \text{ V}$ in

average Vs. Li^+/Li) which has the capacity to be the high energy storage materials^[7]. However, the biggest limit for red phosphorus is its tremendous volume expansion during the process of lithiation-delithiation reaction^[8-9]. Besides, low conductivity is another impedance to be addressed especially under high-rate conditions^[10-11].

To solve these problems, nano-sized red phosphorus particles and their composites with other high conductivity materials (e.g., carbonaceous materials) are supposed to be the most effective approaches to enhance the conductivity. For instance, Liu et al encapsulated nanosized red phosphorus into hierarchical porous carbon nanospheres through a vaporization–condensation process, achieving a high capacity of $2463.8 \text{ mAh g}^{-1}$ at 0.1 A g^{-1} and a decent rate performance of 842.2 mAh g^{-1} at 10 A g^{-1} . Jiao et al reported synthesis of red phosphorus/crumpled nitrogen-doped graphene nanocomposites through a ball-milling process with a high capacity of $2522.6 \text{ mAh g}^{-1}$ at 130 mA g^{-1} , a great cyclability of $1470.1 \text{ mAh g}^{-1}$ at 1300 mA g^{-1} for 300 cycles as well as a satisfactory rate capacity of $1340.5 \text{ mAh g}^{-1}$ at 3900 mA g^{-1} ^[12-13].

Herein, B, N co-doped carbon tube with P encapsulated into the 3D graphene (GO) aerogel network

(3D BN-CT@P@GA) was fabricated. Taking advantages of the BN-doped carbon tube as the P carrier (BN-CT@P), the BN-CT@P was well composited with GA. The B, N-doped hollow carbon tube increased the specific surface area, shortened the ion transmission path, and improved the Li⁺ kinetics. P source was further stabilized after composited with GO in which it not only tightly contacted on the BN-CT but also is protected by rGO layer. As a result, the 3D BN-CT@P@GA possessed excellent cycle stability that delivered reversible $\sim 750 \text{ mAh g}^{-1}$ at 500 mA g^{-1} for 500 cycles.

2 Experimental section

Briefly, urea, polyethylene glycol (PEO, Mw = 4000 M), boric acid and red phosphorus were purchased from Aladdin. The hydrochloric acid, ethanediamine were purchased from Macklin. All the medicines were use directly without further purification.

2.1 Synthesis of BN-CT

Briefly, 5.0 g urea and 0.5 g PEO were added into deionized water (50 mL) and stirred for 10 min at a proper rate. After that, 0.5 g boric acid was supplied in the beaker. The pH value of the precursor solution was tuned to ~ 3 with hydrochloric acid and stirred for another 30 min. Next, the precursor solution was transferred into the oven at the 120°C to finish the evaporation and crosslinking. Then, the cross-linked white solid was transferred into the porcelain with the small window at the temperature 600°C in the nitrogen gas (5°C min^{-1}). Finally, the BN-carbon tube (BN-CT) were prepared.

2.2 Synthesis of BN-CT@P

The BN-CT@P was prepared by vacuum evaporation deposition method. Typically, 0.02 g BN-CT and 0.05 g red phosphorus were mixed together and loaded into the glass tube with the diameter of 0.6 cm in argon atmosphere and annealed at 460°C for 3 h and provided cooling time for 20 h for phase conversion. Finally, the composite was washed using CS₂ solvent to form a pure surface.

2.3 Synthesis of 3D BN-CT@P@GA

0.2 g BN-CT@P, 0.05 g GO and 60 μL ethanediamine were dissolved into 10 mL water in 20 mL capacity glass vial. Then, the vial was transferred into oven and reacted for 8 h at 180 °C.

2.4 Materials characterizations

The phase and morphology of the prepared products were characterized by using an X-ray diffractometer (PXRD, Smartlab) and a scanning electron microscopy (10 kV, FESEM, HITACHI SU8010).

2.5 Electrochemical measurements

The electrochemical capacities were evaluated by

assembled coin-type lithium ion cell. Metallic lithium foil was used as the counter electrode and a polypropylene microporous membrane (Celgard 2400) was used as the separator. The BN-CT@P@GA anodes were coated on Cu foil with the staff mass ratio of 8:1:1 (BN-CT@P@GA powder/acetylene black/ Super P). The final specific capacity was calculated based on the quality of active materials on copper ($\sim 1 \text{ mg}$). After drying for 12 h at the temperature 80°C in the vacuum oven, the final electrodes were obtained using a compact and precision disc cutter (MSK-T-10, MTI Corporation). The electrolyte was composed of 1 M LiPF₆-ethylene carbonate (EC)- dimethyl carbonate (DMC)-ethylmethyl carbonate (EMC) (1 : 1 : 1 by volume). Coin cells were assembled using a compact hydraulic crimping machine (MSK-110, MTI Corporation) in an argon-filled glove-box (Universal 2400/750/900, MIKROUNA) with oxygen and water value lower than 0.1 ppm. The galvanostatic charge–discharge (GCD) tests of BN-CT@P@GA were carried out using a battery testing system LAND CT2001 (Wuhan LAND electronics, China) with a cutoff voltage range from 0.01 V to 2.5 V (vs. Li⁺/Li). For the electrochemical impedance spectroscopy (EIS) measurements, the frequency ranged from 0.01 kHz to 100 Hz.

3 Results and discussion

Figure 1 illustrates the synthesis process of 3D BN-CT@P@GA. The BN-CT is prepared after heating. In the typical process, the assembled carbon tubes as the P carrier derive from the PEO and the heteroatoms originate from boric acid and itself. As known, heteroatoms such as N, B and P can adjust local charge redistribution in carbon-base materials, which can form the center of negative charge and hence bring in the pseudo capacitance effect to increases the capacity. Next, P species are loaded on BN-CT by using the evaporation-deposition method in the inert protect gas. After that, in order to protect the active materials P and provide good electrical conductivity, reductive graphene aerogel network is designed with hydrothermal and freeze drying to encapsule the BN-CT@P. The resultant BN-CT@P@GA shows the freestanding feature and ensures the structural integrity of BN-CT@P.

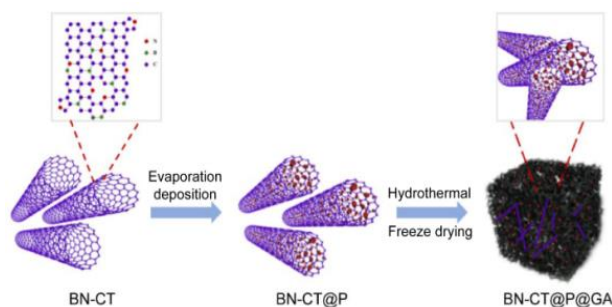


Figure 1 The synthesis procedure of the 3D BN-CT@P@GA

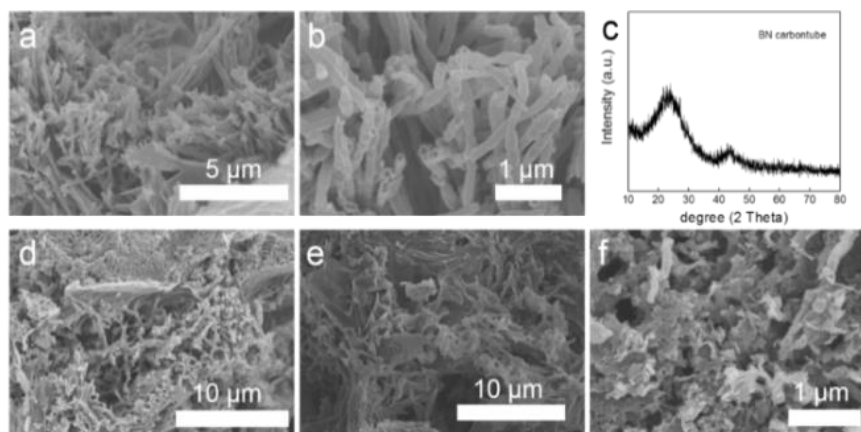


Figure 2 SEM images of BN-CT under different annealing conditions: (a-b) the resulted BN-CT at 850°C, namely, BN-CT-850, (c) XRD pattern of BN-CT-850, (d) BN-CT-700, (e) BN-CT-900, (f) BN-CT-1000

The BN-CT is obtained by simple and scalable annealing method. Figure 2 shows SEM images prepared at different temperatures (BN-CT-X, X represents the temperature). The uniform hollow BN carbon tubes (BN-CT) were successfully synthesized after optimized the temperature to 850°C (BN-CT-850). The XRD pattern shows two diffraction peaks at approximately 23° and 43°, which corresponds to (002) and (100) lattice planes, respectively (Figure 2c). This result indicates that the BN-CT-850 is amorphous^[14]. From HRTEM (Figure S1), the crystalline of the carbon tube is confirmed by the

obvious (002) lattice. It is worth mentioning that the temperature is a crucial factor for the formation of BN-CT. When precursor is reacted at 700°C, only incomplete carbon tubes are formed and separate tiny particles are appeared (Figure 2d). When the temperature increases to 900°C, carbon tubes partly disappear along with the formation of the ultra-thin nanosheets (Figure 2e). When continue to heat up to 1000°C, the carbon tubes link up and turn into the carbonsheets (Figure 2f). This means the BN-CT nanostructure is obtained only at the proper temperature of 850°C.

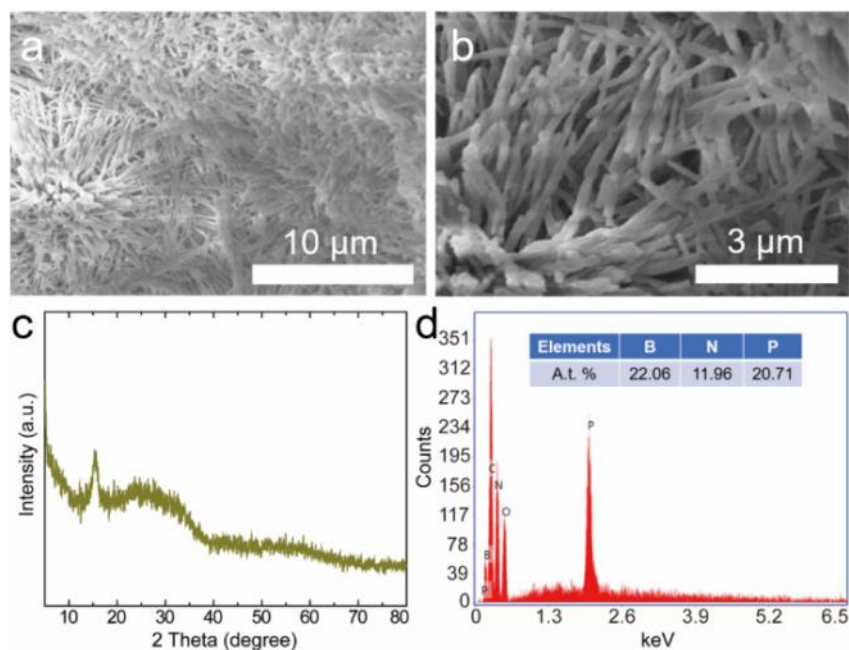


Figure 3 (a-b) The SEM images of BN-CT@P with scales of 10 μm and 3 μm. (c) The XRD pattern of BN-CT@P. (d) The energy dispersive spectrum (EDS) of BN-CT@P, confirming the formation of BN-CT@P

The SEM images of phosphatized BN-CT (BN-CT@P) (Figure 3a-b) exhibit the initial BN carbon tubes morphology, indicating the structure isn't damaged during the phosphating process. As confirmed in XRD pattern, three broadened diffraction peaks located at 13-16°, 25-38°, and 47-65° are consistent with the reported

phosphorus-related works (Figure 3c)^[15]. In addition, the energy dispersive spectrum (EDS) image identifies that the B, N and P species are uniformly distributed with the content of 22.06 %, 11.96 % and 20.71 %, respectively (Figure 3d and the inset Table). The XPS full spectrum also shows B and N successfully doped in carbon tube (Figure S2).

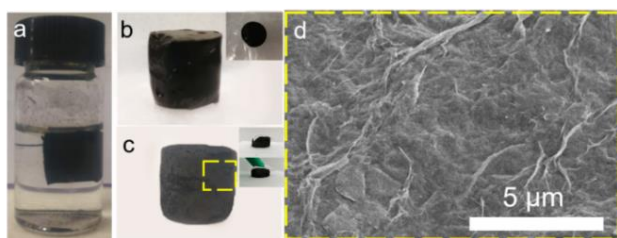


Figure 4 (a-b) Photos of BN-CT@P@GA after hydrothermal reaction. (c) The BN-CT@P@GA exhibit its toughness after free-dried process when given the tough press (insets). (d) The SEM image of BN-CT@P@GA, indicating that the rGO nanosheets cover the surface and protect the structural integrity of BN-CT@P

During hydrothermal reaction with the proper amount precursors, the assembled 3D BN-CT@P-graphene aerogel is prepared (Figure 4a-b) with the diameter of 1.7 cm (inset in Figure 4b). The 3D structure is well reserved and shows the toughness after free-dried process. Figure 4d (the microscopic amplification of BN-CT@P-graphene aerogel) shows the thin rGO nanosheets cover on the surface of BN-CT@P and protect the structure integrity, which alleviate the structure pulverization and deactivation of the active material caused by volume expansion. Especially, when given strong press ($\sim 1 \text{ N cm}^{-2}$) to the BN-CT@P@GA, it still maintains the structure integrity as shown inset of Figure 4c.

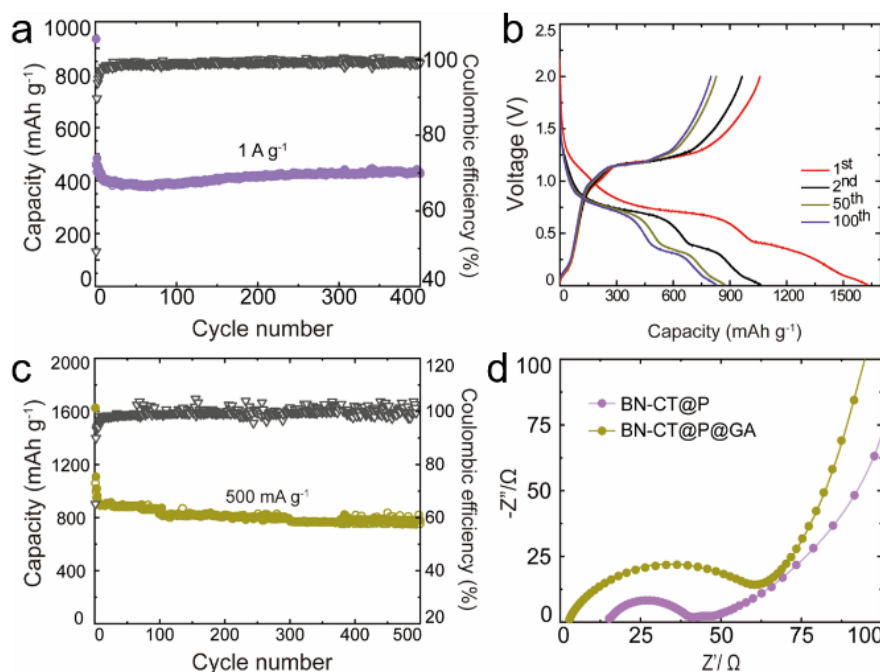


Figure 5 (a) The cyclic performance chart of BN-CT at 1 A g^{-1} . (b) GCD curves for the different cycles. (c) The cyclic performance chart of BN-CT@P@GA at 500 mA g^{-1} . (d) The EIS of BN-CT@P and BN-CT@P@GA

The electrochemical performance of the BN-CT was evaluated at 1 A g^{-1} . The BN-CT anode delivers a better cycling and maintains a stability capacity of 430 mAh g^{-1} after 400 cycles with an average capacity fading only 0.075% per cycle (Figure 5a). It keeps the nature stability of carbon-based materials^[16-18]. After loading P and composited with GO, the capacity shows obvious enhancement (Figure 5b). There is a distinct discharge platform $\sim 0.7 \text{ V}$ that indicates the capacity contribution of P species^[19]. Favorable curve repeatability after 100 cycles shows the BN-CT@P@GA can deliver the reversible performance resulting from its structure.

Moreover, the prolonged cycling performance of BN-CT@P@GA at 500 mA g^{-1} is detected. The initial Coulombic efficiency (ICE) is 65% which is mostly attributed to the formation of SEI from the side reactions of electrolyte on the BN-CT@P@GA surface^[20-21]. After the formation of SEI, the maintained capacity ~ 800

mAh g^{-1} is delivered with no fluctuation (Figure 5c). These results demonstrate that fabrication of BN-CT@P@GA composite is an effective strategy to fix the P species in the skeleton and makes it possible to apply in the energy storage system. The EIS of BN-CT@P and BN-CT@P@GA are exhibited in Figure 5d. Both of them are composed of the semicircle in the high-frequency areas and a liner in the low-frequency areas. The high-frequency area is related to the internal resistance (including separator, electrode/electrolyte and the electrical contact). From Figure 5d, the BN-CT@P shows the smaller internal resistance, indicating the better electron transportation. However, steeper slope at the low-frequency of the BN-CT@P@GA confirms the higher Li^+ diffusivity on the electrolyte-electrode interface. It shows that BN-CT@P@GA material as LIB anode has high rate performance. Figure 6 shows the morphology of BN-CT@P@GA after disassemble the

battery. The BN-CT@P still encapsulate in the graphene network and the whole structure maintains integrity, indicating a highly stable constructing for lithium ions.

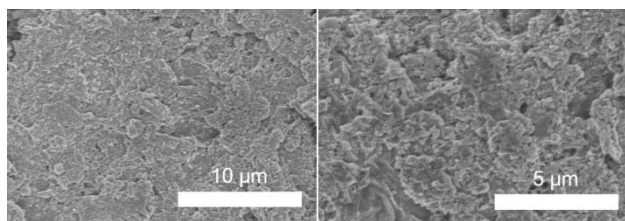


Figure 6 The SEM images of BN-CT@P@GA after 200 cycles at 500 mA g⁻¹

4 Conclusion

In summary, an interesting 3D BN-CT@P@GA skeleton is achieved successfully to protect the active mass P from volume expansion pulverization deactivation. Meantime, a new route to fabricate the double protected network of P is developed (BN-CT carrier effect and graphene aerogel reinforcement effect). Benefiting from the open and connected space of carbon skeleton, the fabricated 3D BN-CT@P@GA sample shows an improved structural stability during the charge-discharge process. As the anode of LIBs, it can deliver a high reversible capacity ~800 mAh g⁻¹ at 500 mA g⁻¹ and excellent cycling stability for 500 cycles. Therefore, this work may offer a novel strategy for rational design of high-performance electrode materials for Li⁺-based energy storage devices.

Author Contributions: F.F. Xu and J Lin contributed equally to this work. F.F. Xu performed the whole experiment including samples preparation, electrode preparation, the cell assembly in a glove box and the measurement of electrochemical properties of the cycling and rate performance, the CV curves, the EIS test. J Lin helped to characterize the morphology features such as SEM, TEM and XRD measurements and analyse the obtained results. Professor H.Z. Sun and C.Y. Tong conducted this whole paper.

Conflict of Interest: No conflict of interest was reported by the authors.

Acknowledgments: Financial supports from the NSFC (22035001, 21574018, and 51433003), the Fundamental Research Funds for the Central Universities (2412019ZD002).

References

- [1] Jiang Y, Wen J, Ding Z, et al. Li⁺ storage properties of SiO₂@C core-shell submicrosphere and its hollow counterpart synthesized by molecular self-assembly in wet-chemistry condition as anodes for LIBs. *Journal of Alloys and Compounds*, 2021; 861.
- [2] Lopez J, Gonzalez R, Ayala J, et al. Centrifugally spun TiO₂/C composite fibers prepared from TiS₂/PAN precursor fibers as binder-free anodes for LIBs. *Journal of Physics and Chemistry of Solids*, 2021; 149.
- [3] Zhang X, Qiu Y, Cheng F, et al. Realization of a High-Voltage and High-Rate Nickel-Rich NCM Cathode Material for LIBs by Co and Ti Dual Modification. *ACS Appl Mater Interfaces*, 2021, 13 (15): 17707-17716.
- [4] Rabiei Baboukani A, Khakpour I, Adelowo E, et al. High-performance red phosphorus-sulfurized polyacrylonitrile composite by electrostatic spray deposition for lithium-ion batteries. *Electrochimica Acta*, 2020; 345.
- [5] Liang S, Pei X, Jiang W, et al. Free standing dual-network red phosphorus@porous multichannel carbon nanofibers/carbon nanotubes as a stable anode for lithium-ion batteries. *Electrochimica Acta*, 2019, 322: 134696.
- [6] Xue J, Wang D, Xia X, et al. Confined red phosphorus in N-doped hierarchically porous carbon for lithium ion batteries with enhanced rate capability and cycle stability. *Microporous and Mesoporous Materials*, 2020, 305.
- [7] Wu K, Xu G, Pan D, et al. Red phosphorus confined in MOF-derived N-doped carbon-based composite polyhedrons on carbon nanotubes for high-areal-capacity lithium storage. *Chemical Engineering Journal*, 2020, 385: 123456.
- [8] Chen X, Qiu J, Wang Y, et al. A stable polypyridinopyridine-red phosphorus composite as a superior anode material for long-cycle lifetime lithium-ion batteries. *New Journal of Chemistry*, 2019, 43 (16): 6197-6204.
- [9] Yan Y, Xu H, Peng C, et al. 3D phosphorus-carbon electrode with aligned nanochannels promise high-areal-capacity and cyclability in lithium-ion battery. *Applied Surface Science*, 2019, 489: 734-740.
- [10] Zhang Y, Sun L, Zhao X, et al. Construction of Sn-P-graphene microstructure with Sn-C and P-C co-bonding as anodes for lithium-ion batteries. *Chem Commun (Camb)*, 2020, 56 (72): 10572-10575.
- [11] Liu H, Zhang S, Zhu Q, et al. Fluffy carbon-coated red phosphorus as a highly stable and high-rate anode for lithium-ion batteries. *Journal of Materials Chemistry A*, 2019, 7 (18): 11205-11213.
- [12] Liu B, Zhang Q, Li L, et al. Encapsulating Red Phosphorus in Ultralarge Pore Volume Hierarchical Porous Carbon Nanospheres for Lithium/Sodium-Ion Half/Full Batteries. *ACS Nano*, 2019, 13 (11): 13513-13523.
- [13] Jiao X, Liu Y, Li T, et al. Crumpled Nitrogen-Doped Graphene-Wrapped Phosphorus Composite as a Promising Anode for Lithium-Ion Batteries. *ACS Appl Mater Interfaces*, 2019, 11 (34): 30858-30864.
- [14] Yang H, Zhou J, Wang M, et al. From basil seed to flexible supercapacitors: Green synthesis of heteroatom-enriched porous carbon by self-gelation strategy. *International Journal of Energy Research*, 2020, 44 (6):

4449-4463.

- [15] Chang W. C, Tseng K. W, Tuan H. Y. Solution Synthesis of Iodine-Doped Red Phosphorus Nanoparticles for Lithium-Ion Battery Anodes. *Nano Lett*, 2017, 17(2): 1240-1247.
- [16] Kong W, Yu J, Shi X, et al. Encapsulated Red Phosphorus in rGO-C₃N₄ Architecture as Extending-Life Anode Materials for Lithium-Ion Batteries. *Journal of The Electrochemical Society*, 2020, 167 (6).
- [17] Shen J, Wang Y, Yao Y, et al. Flexible Free-Standing Hierarchical Carbon-Coated CoP₂ Nanosheets for High-Performance Lithium-Ion Batteries. *ACS Applied Energy Materials*, 2018; 1 (12), 7253-7262.
- [18] Wang L, Ju J, Deng N, et al. Embedding red phosphorus in hierarchical porous carbon nanofibers as anodes for lithium-ion battery. *Materials Letters*, 2019, 240: 39-43.
- [19] Wang T, Wei S, Villegas Salvatierra R, et al. Tip-Sonicated Red Phosphorus-Graphene Nanoribbon Composite for Full Lithium-Ion Batteries. *ACS Appl Mater Interfaces*, 2018, 10 (45): 38936-38943.
- [20] Jiao X, Liu Y, Li B, et al. Amorphous phosphorus-carbon nanotube hybrid anode with ultralong cycle life and high-rate capability for lithium-ion batteries. *Carbon*, 2019, 148: 518-524.
- [21] Zhang S, Liu C, Wang H, et al. A Covalent P-C Bond Stabilizes Red Phosphorus in an Engineered Carbon Host for High-Performance Lithium-Ion Battery Anodes. *ACS Nano*, 2021, 15 (2): 3365-3375.

Synthesis and Mechanical Properties of C/PLA 3D Printing Composites Based on Waste Rice Noodles

Jie YANG, Xinyan JIN, Yan LIU, Shuoping CHEN*

College of Materials Science and Engineering, Guilin University of technology, Guilin 541004, China

*Corresponding author: Shuoping CHEN, E-mail: chenshuoping_777@163.com

Abstract:

Spherical carbon particles were prepared by using waste Guilin rice noodles as raw materials. By blending the rice noodles based carbon (RC) powders with polylactic acid (PLA), A series of black RC/PLA 3D printing composites were synthesized and characterized. The mechanical testing result shows that the RC/PLA 3D printing composites display better mechanical properties than that of pure PLA. Moreover, the composite with carbon treated with high temperature carbonization has better impact strength.

Keywords: Waste Guilin rice noodles; RC/PLA 3D printing composite

1 Introduction

Poly(lactic acid) (PLA) has become one of the most commonly used raw materials for fused deposition molding (FDM) 3D printing, for it has many desirable characteristics such as excellent degradability, good biocompatibility, low warpage, and low shrinkage during FDM molding^[1]. However, the printed products of pure PLA usually display high brittleness and low impact strength, which will limit their wider application^[2-3]. Composite modification with carbon materials is an effective method for improving mechanical properties of PLA, and it has been reported that carbon fibers or carbon nanotubes can substantially enhance the tensile strength, modulus and impact strength of PLA printed products^[4-7]. However, the high prices of carbon fibers or carbon nanotubes (higher than 1000RMB/kg) will increase the cost of carbon/PLA 3D printing composites and are not easy to be popularized.

On the other hand, Guilin rice noodle is a traditional snack and locals' daily diet in Guilin city, China. A large number (about 70 tons) of surplus waste rice noodles are produced every day. Nevertheless, most of the waste rice noodles are used as the raw material of low-margin fermented feed, and the others are abandoned directly, which may cause potential and long-term pollution to the soil and aqueous environment. Thus, it is necessary to explore an effective way for recycling waste rice noodles.

It has been proved that hydrothermal carbonization of many organic wastes can provide cheap biomass

carbon materials^[8-10]. The main constituent of waste Guilin rice noodles is starch (more than 70% at dry weight), which means that waste Guilin rice noodles may be carbonized in hydrothermal conditions and form carbon particles with specific morphology. Thus, to recover waste rice noodles effectively and lower the price of carbon/PLA 3D printing composites, we prepared a kind of carbon material with waste Guilin rice noodles as raw materials (RC) and blended it with PLA, synthesizing a series of low-priced RC/PLA 3D printing composites. The mechanical properties of the resulted RC/PLA 3D printing composites are also investigated in this paper.

2 Experimental section

2.1 Materials.

The polylactic Acid (PLA, 6202D, powder) with a density of 1.24 g/cm³ and a molecular weight of 300000 ~ 320000 g/mol was purchased from NatureWorks LLC, USA. The waste Guilin rice noodle (main organic constituent: Starch 21.36g/100g; Protein 1.91 g/100g; Fat 0.4 g/100g; Water 76.33 g/100g) was collected from the canteen of Guilin University of Technology.

2.2 Preparation of carbon spheres based on waste Guilin rice noodles

10 g waste Guilin rice noodles were grinded to a smooth paste in a mortar, and then mixed with 20 g

deionized water. The resulted mixture was transferred to a 50ml sealed Teflon-lined autoclave, and then heated at 200 °C for 10 hours. After natural cooling, vacuum filtration and drying at 60 °C for 24 hours, black hydrothermal carbon material (RC1) was obtained. The resulted C1 carbon material was high-temperature calcinated at 800 °C for 1 hour under N₂ protection, forming carbon material with full carbonization (RC2).

2.3 Preparation and 3D printing of C/PLA 3D printing composite

3D printing wires of C/PLA composite were produced by a XinShuo WSJXT-12 miniature single screw extruder. At first, carbon powders (RC1 or RC2) were mixed with PLA powder with a certain mass ratio (1:99, 2:98, 3:97, 4:96 or 5:95) and then dried at 60 °C for 12 hours, respectively. The resulted RC/PLA mixture was added to the miniature single screw extruder with a feed inlet temperature of 70 °C, a screw area temperature of 160 °C and a discharge outlet temperature of 80 °C. The semi-molten RC/PLA composite was extruded from the discharge port, drawn through the circulating water cooling tank and then introduced into the silk collector. When the screw speed, traction speed and silk collector speed were adjusted to 42 rpm, 170 rpm and 7 rpm respectively, black 3D printing wires of RC/PLA composite with a diameter of 1.75 mm ± 0.1 mm were obtained (See Figure 1a).

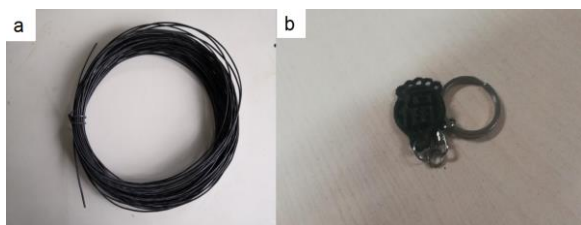


Figure 1 Photos of 3D printing wires (a) and 3D printed key chain (b) of RC/PLA composite

3D printing of RC/PLA 3D printing composite was carried out in a JG-Maker A3 FDM 3D printer, with an extrusion head temperature of 200 °C, a bed temperature of 50 °C, and a printing speed of 50 mm/s. The 3D printed product was a kind of black solid (See Figure 1b).

2.4 Characterization

The powder X-ray diffraction (PXRD) patterns were obtained with a PANalytical X'pert PRO X-ray diffractometer with Cu K α radiation ($\lambda = 0.15418 \text{ \AA}$) at 40 kV and 40 mA and a scan speed of 4 ° min⁻¹ (2 θ). The Infrared (IR) spectrum was recorded as KBr pellets at a range of 400-4000cm⁻¹ on a Nicolet 5700 FT-IR spectrometer with a spectral resolution of 4.00 cm⁻¹. The morphology of the resulted carbon powders were characterized by using an S-4800 field emission scanning electron microscope (SEM), The IZOD impact strength

of RC/PLA 3D printing composite was measured by a DR-802b cantilever beam impact testing machine with a impact energy of 1J. The tensile properties of RC/PLA 3D printing composite were tested by a UTM4503 electronic universal testing machine with a drawing speed of 1mm/min. All mechanical results presented in this paper represent the average measurement of four samples having the same composition.

3 Result and discussion

3.1 Characterization of carbon materials based on waste Guilin rice noodles

Figure 2a shows the PXRD diagram of carbon materials RC1 and RC2 based on waste Guilin rice noodles. The diffraction peaks around 26 ° and 44 ° could be assigned to (002) and (100) planes of graphite^[11], respectively, which indicated that the resulted carbon materials were partially graphitized. Compared with RC1, the diffraction peaks of (002) planes in RC2 shifted to a higher angle, and the peak of (100) planes was evident, which indicated that calcination at 800 °C could enhance the graphitization of the materials.

The IR spectra of carbon materials RC1 and RC2 were basically similar (See Figure 2b). There were hydrophilic groups like hydroxyl and amino groups on the surface of these carbon particles. The wide absorption peak at about 3420 cm⁻¹ corresponded to the stretching vibration of O-H and N-H bonds, while the bending vibrations of these function groups were located at about 1600cm⁻¹.

Most carbon particles based on waste Guilin rice noodles showed a spherical morphology with a diameter range of 4-30 μm. The surface of RC1 was smooth, while RC2's surface was rough with many small protuberances (See Figure 2c and 2d). The rough surface in RC2 particles could improve the adhesion between the carbon particles and matrix PLA materials and might be advantageous in enhancing the mechanical property.

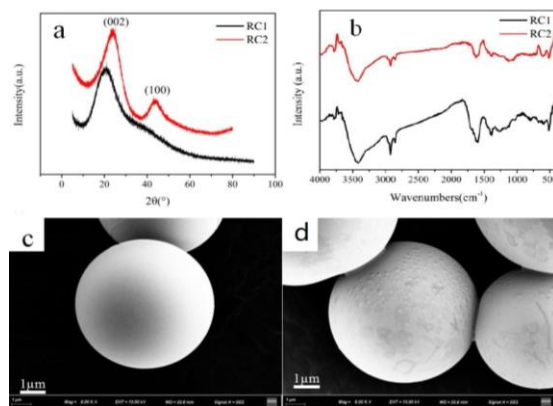


Figure 2 (a) PXRD patterns of carbon materials RC1 and RC2; (b) IR spectra of carbons materials RC1 and RC2; (c)-(d): SEM images of carbon materials RC1(c) and RC2(d)

3.2 Mechanical properties of RC/PLA composites

Figure 3 shows the IZOD impact strength diagram of RC/PLA 3D printing composites. The pure PLA displayed a weak IZOD impact strength of 1.28 kJ/m^2 , which could be improved remarkably by the introduction of RC. The IZOD impact strength of RC1/PLA composites increased with the increasing of RC1 content when the mass fraction of RC1 was not more than 4wt%, while decreased when exceeding this limit. The impact strength of RC1/PLA composite with 4 wt% RC1 was 1.88 kJ/m^2 , which was 47% higher than that of pure PLA (See Figure 3a).

On the other hand, the IZOD impact strength of RC2/PLA composites also increased greatly with the increasing of RC2 addition, while the improvement effect of RC2 on the impact strength of PLA based printing products was much higher than that of RC1. The impact strength of RC2/PLA composites with 5 wt% RC2 was up to 9.68 kJ/m^2 and 7.5 times more than that of pure PLA (See Figure 3b). It might be due to the higher graphitization degree and rough surface of RC2, which could absorb the impact energy and combine with the PLA matrix more effectively.

The introduction of RC could also improve the tensile properties of PLA material. As shown in Figure 4a, with the increasing of RC1, both tensile strength and elongation at break of RC1/PLA composites increased firstly and then decreased. The RC1/PLA composite with 2 wt% RC1 displayed the highest tensile strength of 30.0

MPa and good elongation at break of 18.9%, which were 71% and 154% higher than that of pure PLA, respectively. A similar phenomenon was observed in the RC2/PLA system. However, though with high IZOD impact strength, the RC2/PLA composite contained 5 wt% RC2 displayed relative weak tensile properties (Tensile strength: 19.86MPa; Elongation at break: 10.76%), which was only slightly higher than that of pure PLA.

4 Conclusion

In this paper, we converted Guilin rice noodles to spherical carbon particles (RC), and synthesized a series of black RC/PLA 3D printing composites. The result RC/PLA 3D printing composites have better mechanical properties than pure PLA. In particular, calcinated carbons (RC2) in RC/PLA composites could effectively improve the low impact resistance of the PLA matrix. The RC2/PLA composite containing 5wt% RC2 has outstanding impact strength (9.68 kJ/m^2 , 7.56 times of pure PLA), and its tensile strength (19.86MPa) and elongation at break (10.76%) are also improved compared with that of pure PLA. Such RC/PLA 3D printing composites have a higher added value than that of fermented feed, which could be advantageous for recycling waste rice noodles. On the other hand, due to low-cost carbon particles from waste Guilin rice noodles, the resulted RC/PLA 3D printing composites could also be a new way for low-cost 3D printing.

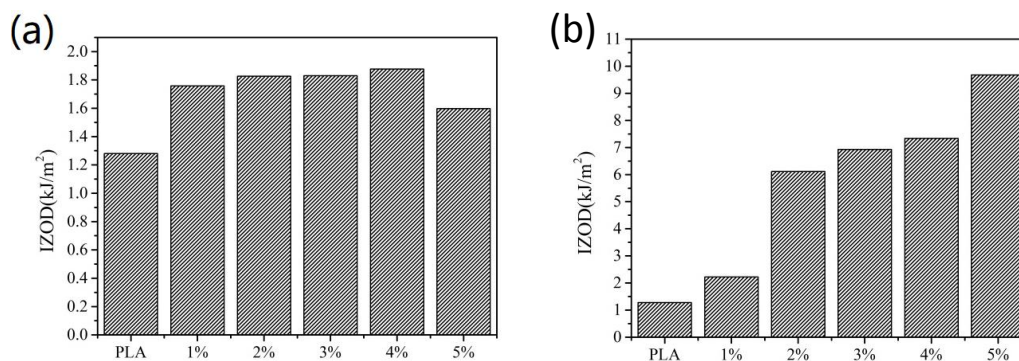


Figure 3 Izod impact strengths of RC/PLA composites with different amount of RC1 (a) and RC2 (b)

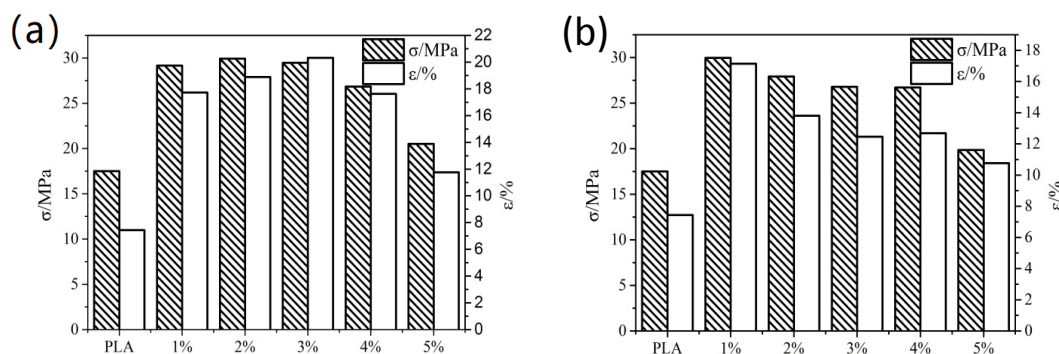


Figure 4 Tensile properties of RC /PLA 3D printing Composites with different amount of RC1 (a) and RC2 (b)

Acknowledgement: This work was supported by grants of the National Nature Science Foundation of China (No. 51763007) and National Undergraduate Innovation and Entrepreneurship Training Program (No. 201910596205).

References

- [1] L Li, Y Chen, T Yu, N. Wang, C. Wang, H. Wang, Preparation of polylactic acid/TEMPO-oxidized bacterial cellulose nanocomposites for 3D printing via Pickering emulsion approach, *Composites Communications*, 2019, 16: 162-167.
- [2] C Murphy, M N Collins. Microcrystalline cellulose reinforced polylactic acid biocomposite filaments for 3D printing, *Polymer Composites*, 2016, 39: 1311-1320.
- [3] D H Rosenzweig, E Carelli, T Steffen, et al. 3D-Printed ABS and PLA Scaffolds for Cartilage and Nucleus Pulposus Tissue Regeneration, *International journal of molecular sciences*, 2015, 16: 15118-15135.
- [4] Y Zhou, L Lei, B Yang, et al. Preparation and characterization of polylactic acid (PLA) carbon nanotube nanocomposites. *Polymer Testing*, 2018, 68: 34-38.
- [5] H S Patanwala, D Hong, S R Vora, et al. The microstructure and mechanical properties of 3D printed carbon nanotube-polylactic acid composites. *Polymer Composites*, 2018, 39: E1060-E1071.
- [6] R Chen, M Misra, A K Mohanty. Injection-moulded biocomposites from polylactic acid (PLA) and recycled carbon fibre: Evaluation of mechanical and thermal properties. *Journal of Thermoplastic Composite Materials*, 2014, 27 (9): 1286-1300.
- [7] C T Hsieh, Y J Pan, C W Lou, et al. Polylactic Acid/Carbon Fiber Composites: Effects of Functionalized Elastomers on Mechanical Properties, Thermal Behavior, Surface Compatibility, and Electrical Characteristics. *Fibers and Polymers*, 2016, 17 (4): 615-623.
- [8] J Wei, H Wang, Q Zhang, et al. One-pot Hydrothermal Synthesis of N-Doped Carbon Quantum Dots Using the Waste of Shrimp for Hydrogen Evolution from Formic Acid. *Chemistry Letters*, 2015, 44 (3): 241-243.
- [9] F Li, Y Tang, H Wang, et al. Functionalized hydrothermal carbon derived from waste pomelo peel as solid-phase extractant for the removal of uranyl from aqueous solution. *Environmental Science and Pollution Research*, 2017, 24 (28): 22321-22331.
- [10] A Jain, R Balasubramanian, M P Srinivasan. Production of high surface area mesoporous activated carbons from waste biomass using hydrogen peroxide-mediated hydrothermal treatment for adsorption applications. *Chemical Engineering Journal*, 2015, 273: 622-629.
- [11] H Abdolmohammad Zadeh, E Rahimpour. A novel chemosensor based on graphitic carbon nitride quantum dots and potassium ferricyanide chemiluminescence system for Hg(II) ion detection. *Sensors and Actuators B: Chemical*, 2016, 225: 258-266.

A Novel Preparation Method of Organic-inorganic Aramid Nanofibers (ANFs) Hybrid Membrane Using Ethanol as Proton Donor

Shengjun LU

College of Materials and Metallurgy, Guizhou University, Guiyang, Guizhou, 550025, China

*Corresponding author: Shengjun LU, Email: sjlu@gzu.edu.cn

Abstract:

In the work, the surface of the titanium dioxide (TiO_2) nano particles were modified with 3-Aminopropyltriethoxysilane (KH550) first. And the ANFs were loaded with the different nano TiO_2 assisted via the ultrasonic process. Then the organic and inorganic hybrid membrane were fabrication by vacuum assisted flocculation (VAF). Ethanol as a proton donor can realize the flocculation of ANFs. The results of the nanocomposites were characterized by Transmission electron microscope (TEM), X-ray diffraction (XRD), and scanning electron microscopy (SEM). The SEM results indicated that the agglomeration of nanoparticles on ANF were reduced obviously, Through the preparation of aramid nanofiber membrane with the proton donor of ethanol, it is observed that the interlaced network structures of the membrane surface were constructed. The result of the UV data is that the addition of nano-titanium dioxide improves the UV absorption capacity of the fiber membrane.

Keywords: Aramid nanofiber; Nano- TiO_2 ; Hybridization; Functional; Nanocomposites

1 Introduction

So far, the preparation of organic-inorganic hybrid composite membranes has been applied to various potential applications^[1-5]. The successful combination of ANFs with gold nanoparticles^[6], carbon nanotubes^[7], graphene and silver nanowires provide new methods for organic-inorganic hybridization of ANFs. Due to the high specific surface area of nanoparticles, agglomeration is a serious problem which make nanoparticles poorly dispersed in the organic matrix. Surface modification of nanoparticles is usually needed to achieve uniform dispersion of nanoparticles. It has been reported that transparent magnetic composite membrane are successfully prepared by combining inorganic magnetic nanoparticles with nano fibrillated cellulose matrix to form a three-dimensional network structure^[8]. There are many active functional groups on the surface of ANFs, which have good adhesion with other nanomaterials. However, the aramid fiber has weak UV resistance, and the composite film prepared by ANFs has poor anti UV resistance. At the same time, Nano- TiO_2 has good UV absorption performance and good binding sites on the surface of ANFs. Combining the two can improve the anti UV performance of the composite film. Inspired by

the combination of nano fibrillated cellulose and nano particles, it becomes feasible to combine ANFs with functionalized inorganic nanoparticles to obtain hybrid films with anti UV resistance.

In this work, Nano- TiO_2 and ANFs are proposed to be combined to prepare TiO_2 /ANFs. Then the TiO_2 /ANFs hybrid films are fabricated by vacuum flocculation with ethanol as proton donor. After surface modification of Nano- TiO_2 by KH550, inorganic nanoparticles are able to disperse in ethanol uniformly. In addition, uniformly distributed nano-sized TiO_2 particles also endow the nano-sized TiO_2 /ANFs with good anti-ultraviolet properties.

2 Experimental section

2.1 Materials

Aramid fiber (Kevlar-29): Model 956, specification 1500D, linear density 1670 dtex, was purchased from Dupont Company, USA. Potassium hydroxide (KOH), and Dimethyl sulfoxide (DMSO, 99.7%) were purchased from Aladdin co., Ltd, Shanghai, China. Ethanol (density (20 °C) is 0.789~0.791 g/ml, grade is analytical grade (AR), content $\geq 99.7\%$) were supplied by Fuyu Chemical, Tianjin, China. Nano Titanium dioxide (TiO_2 ,

content 99.8%, particle size of 25 nm) were purchased from Macklin co., Ltd, Shanghai, China.

2.2 Sample preparation

2.2.1 Preparation of ANFs/DMSO suspension

1.5g KOH was dissolved in the DMSO, and 1.5g clean aramid fiber was added in the DMSO solution. Then the dark red ANFs solution was formed by continuous stirring at 25 °C for one week.

2.2.2 Surface modification treatment of Nano-TiO₂

The ethanol absolute, deionized water and KH550 were mixed with a fixed ratio (90:10:1 ml) and place in the flask. The mixture was disposed by ultrasonic for 10 minutes. The pH was adjusted at 4 by adding adequate hydrochloric acid and sodium hydroxide [9]. Subsequently, A certain amount of well dispersed KH550 was added into the mixture dispersed Nano-TiO₂, stirring for one hour in the oil bath at the temperature of 60 °C. Then the excess KH550 was removed by deionized water and ethanol washing for several times. At last the treated TiO₂ nanoparticles were dried in the vacuum oven at 100 °C for 6 h. In short, the original sample was named as U-TiO₂ and the KH550-modified Nano-TiO₂ was named as T-TiO₂.

2.2.3 Fabrication TiO₂/ANFs nanocomposites

20 ml of ANFs/DMSO solution were added into 100 ml of ethanol solution and an ultrasonic treatment of 2 hours were proceed to obtain uniform suspensions. Then ANFs membrane were fabricated by vacuum assisted flocculation method. In the process of suction filtration, washing with ethanol were used to remove DMSO solution, and the vacuum suction filtration for 6~8 h was also applied to obtain uniform and transparent ANF membrane. The same method was also used to prepare Nanocomposites with different mass fractions of nano TiO₂ particles. Then ANFs/DMSO and TiO₂ were dispersed and ultrasonic processed in the ethanol together with different weight ratio. Finally, the films were dried in a vacuum oven at 60 °C for 8 hours.

2.3 Characterization

A scanning electron microscope (SU8010 and JEOL JSM-7500F) was used to observe the surface morphology of TiO₂ and TiO₂/ANFs. The TEM (FEI Tecnai G2 F20) was applied to observe the morphology of ANFs. An UV-vis spectrophotometer (PE Lambda 950) was used to evaluate the absorption properties of the nano paper in the wavelength range of 200~800 nm.

3 Results and discussion

3.1 Morphologies of TiO₂ and ANF

According to the SEM results in Figure 1(a) (b), it is observed that the agglomeration of nanoparticles has been significantly reduced after the treatment of silane coupling agent. Via grafting silane coupling agent on the

surface, the nano particles are well dispersed, providing a good precondition for the preparation of uniform and dense nano composite membrane. In Figure 1(c) (d), it can be concluded from the TEM results that ANFs with the size of nanometer have been successfully prepared. After mixing the modified nano particles with ANFs, it is observed that nano particles are uniformly attached on the surface of the nanofibers, conforming to our assumptive scheme of organic and inorganic nano paper in Figure 2. In Figure 2, There is a hydrogen bond between the carbonyl group on the fiber surface and the amino group between the nanoparticles. So that the nanoparticles can be stably dispersed in the suspension of ANFs [8].

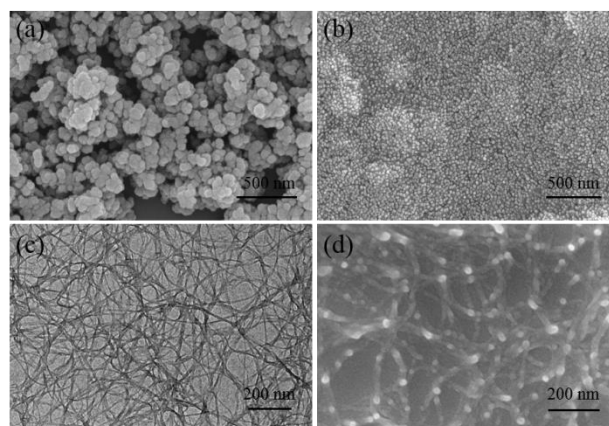


Figure 1 SEM images of the TiO₂ (a) U-TiO₂, (b) T-TiO₂, (c) TEM photographs of the ANFs, (d) Combination of ANFs and nanoparticles

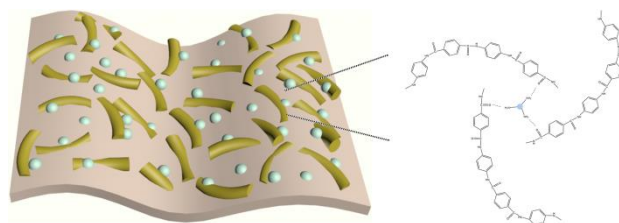


Figure 2 Schematic diagram of organic inorganic nanocomposite paper

3.2 XRD patterns and UV absorption properties of nano hybrid films

Due to the entanglement network of aramid fibers constructed by the strong hydrogen bond among molecules, the size of ANFs is far smaller than the wavelength of visible light, leading a good transparency of the ANFs membrane. From the XRD results of ANF and hybrid films in Figure 3(a), it can be seen that the ANFs film keeps the crystal surface and crystallinity of the traditional aramid fiber. Specifically, ANFs membrane maintains the peak of macro fiber at about 20~30 °, which corresponds to the (110), (200), and (004) lattice planes of Kevlar fibers. The nanoparticles are uniformly distributed on nanofibers through chemical

bonding and electrostatic adsorption. In Figure 3(b), the pure ANFs film has a transmittance of over 80% of the visible light, showing a high transparency. It is attributed to the smaller size than the visible light wavelength of the ANFs. When inorganic nanoparticles are attached to

the hybrid membrane, the network structure is formed between the nanofibers and the nanoparticles, and the fibers and the nanoparticles are more closely combined, so the transparency decreased significantly.

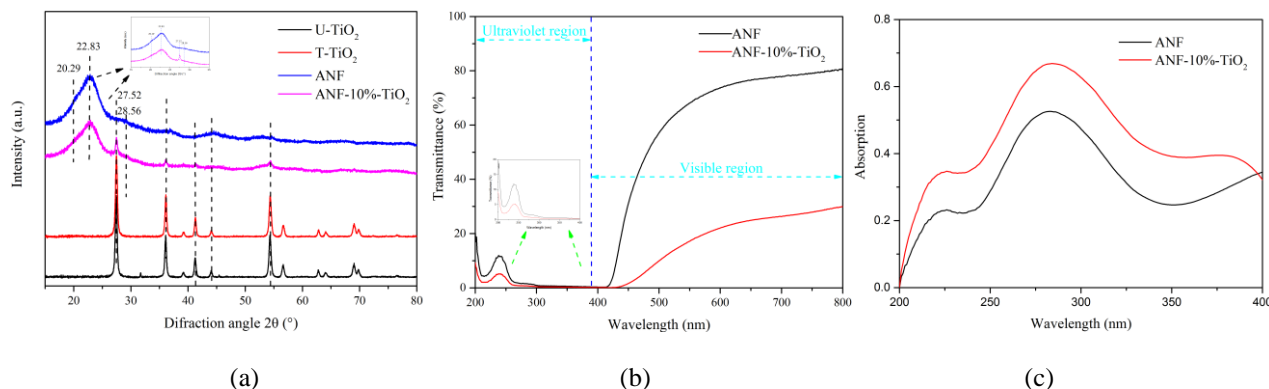


Figure 3 (a) XRD patterns of nanoparticles and nanocomposite films, (b) Transmission of pure ANFs and hybrid membranes, (c) Absorption spectra of pure ANFs membrane and hybrid membrane

As shown in Figure 3c, the hybrid film with 10% nano particles has a higher absorption intensity in the range of 200~400 nm than the pure ANF film, showing a better UV absorption capacity, which is attributed to the nano TiO₂ as the oxide semiconductor. Nano TiO₂ can absorb ultraviolet light to produce electron/hole pairs, TiO₂ absorbs ultraviolet energy and its electrons are excited from the valence band to the conduction band. The formation of conduction band may be involved in the recombination process or the redox reaction on the surface of TiO₂. The UV energy consumption by TiO₂ can protect the material from UV [10-13]. The optical band gap of Nano-TiO₂ is 385 nm (3.2eV), and below 350 nm it has a strong absorption intensity. The improvement of UV absorption capacity will make the fiber membrane have a better application in the field of UV resistance.

4 Conclusions

In a word, the modified nanoparticles are fixed in the network of ANFs to prepare organic-inorganic hybrid films. The transparency of hybrid membrane depends on the amounts of nano particles attached. Therefore, in the process of preparing composite membranes, it can effectively promote the close bonding of inorganic nanoparticles and ANFs, and prepare uniform and compact composite membranes. The obtained hybrid film has certain transparency, and the pure aramid nanofilm has a transmittance of 80 % in the visible light range. This kind of organic-inorganic hybrid membrane with certain UV absorption effect can be obtained through relatively simple processing and preparation process. This novel method can be an inspiration to the application of organic-inorganic hybrid functionalized composites.

no known competing financial interests or personal relationships that could have appeared to influence the work reported in this paper.

Acknowledgements: This work was supported by the Guizhou Province "100-level" Innovative Talents Project, Qianke Union platform talent (NO. [2016] 5653).

References

- [1] X b Yin, Feng X. Organic-Inorganic Hybrid Membranes for Proton Exchange Membrane Fuel Cells [J]. *Current Organic Chemistry*, 2014, 18(18):2405-2414. <http://doi.org/10.2174/1385272819666140806202329>.
- [2] Tripathi B P, Shahi V K. Organic-inorganic nanocomposite polymer electrolyte membranes for fuel cell applications[J]. *Progress in Polymer Science*, 2011, 36(7): 945-979. <http://doi.org/10.1016/j.progpolymsci.2010.12.005>.
- [3] de Oliveira R L, da Silva Barud H, De Salvi D T B, et al. Transparent organic-inorganic nanocomposites membranes based on carboxymethylcellulose and synthetic clay[J]. *Industrial Crops and Products*, 2015, 69: 415-423. <http://doi.org/10.1016/j.indcrop.2015.02.015>.
- [4] Tripathi B P, Kumar M, Saxena A, et al. Bifunctionalized organic-inorganic charged nanocomposite membrane for pervaporation dehydration of ethanol[J]. *Journal of colloid and interface science*, 2010, 346(1): 54-60. <http://doi.org/10.1016/j.jcis.2010.02.022>.
- [5] Yang H C, Hou J, Chen V, et al. Surface and interface engineering for organic-inorganic composite membranes[J]. *Journal of Materials Chemistry A*, 2016, 4(25): 9716-9729. <http://doi.org/10.1039/c6ta02844f>.
- [6] Lyu J, Wang X, Liu L, et al. High strength conductive composites with plasmonic nanoparticles aligned on aramid nanofibers[J]. *Advanced Functional Materials*, 2016, 26(46): 8435-8445.

Conflict of interest: The authors declare that they have

<http://doi.org/10.1002/adfm.201603230>.

- [7] Zhu J, Cao W, Yue M, et al. Strong and stiff aramid nanofiber/carbon nanotube nanocomposites [J]. *ACS nano*, 2015, 9(3): 2489-2501. <http://doi.org/10.1021/nn504927e>.
- [8] Li Y, Zhu H, Gu H, et al. Strong transparent magnetic nanopaper prepared by immobilization of Fe_3O_4 nanoparticles in a nanofibrillated cellulose network[J]. *Journal of Materials Chemistry A*, 2013, 1(48): 15278-15283. <http://doi.org/10.1039/c3ta12591b>.
- [9] Mallakpour S, Barati A. Efficient preparation of hybrid nanocomposite coatings based on poly (vinyl alcohol) and silane coupling agent modified TiO_2 nanoparticles[J]. *Progress in Organic Coatings*, 2011, 71(4): 391-398. <http://doi.org/10.1016/j.porgcoat.2011.04.010>.
- [10] Hu J, Gao Q, Xu L, et al. Significant improvement in thermal and UV resistances of UHMWPE fabric through in situ formation of polysiloxane- TiO_2 hybrid layers[J]. *ACS Applied Materials & Interfaces*, 2016, 8(35): 23311-23320. <http://doi.org/10.1021/acsami.6b04914>.
- [11] Popov A P, Priezhev A V, Fedoseeva M S, et al. Calculation of absorption, reflectance, transmission, and depolarization of UV radiation propagating through a layer of suspension of titanium dioxide nanoparticles[J]. *Moscow University Physics Bulletin*, 2009, 64(5): 513-518. <http://doi.org/10.3103/S0027134909050099>.
- [12] Yang H, Zhu S, Ning P. Studying the mechanisms of titanium dioxide as ultraviolet - blocking additive for films and fabrics by an improved scheme [J]. *Journal of Applied Polymer Science*, 2004, 92(5): 3201-3210. <http://doi.org/10.1002/app.20327>.
- [13] Pakdel E, Daoud W A, Wang X. Assimilating the photo-induced functions of TiO_2 -based compounds in textiles: emphasis on the sol-gel process [J]. *Textile Research Journal*, 2014, 85(13): 1404-1428. <http://doi.org/10.1177/0040517514551462>.

Gradient Ultra-fine Grained Surface Layer in 6063 Aluminum Alloy Obtained by Means of Rotational Accelerated Shot Peening

Ying LIU^{1*}, Hailu XU², He XIAN¹, Yanfang LIU¹, Zheng LI^{1*}

1. School of Materials Science and Engineering, Nanjing University of Science and Technology, Nanjing 210094, China,

2. Faculty of Electrical and Mechanical, Pujiang College of Nanjing University of Technology, Nanjing 21100, China

*Corresponding authors: Ying LIU, Zheng LI, Email: liuying517@njust.edu.cn; lizhengnust@foxmail.com

Abstract:

Gradient ultra-fine grained surface layer in 6063 aluminum alloy was obtained by means of a novel surface self-nanocrystallization technique, namely rotational accelerated shot peening (RASP) treatment. The average grain sizes along the vertical section vary from hundreds of nanometers in the top surface to micrometers in the matrix. By using orthogonal experimental design to compare roughness values and hardness values, we synthesized the processing parameters to obtain sample of smaller roughness values and higher hardness.

Keywords: rotational accelerated shot peening; gradient ultra-fine grained structure; orthogonal experimental design; processing parameters

1 Introduction

The major failure modes of metallic engineering materials are fracture, corrosion and wear, which occurred or originated from the surface of materials. Therefore, it is significant to change surface micro-structures and compositions via physical and chemical techniques to satisfy the industrial requirements for the surface properties^[1].

In 1999, Lu K^[2] combined the thought of the nano-structure with metal materials, put forward the surface nanocrystallization (SNC) concept, which through a certain physical or chemical methods, preparation of a surface layer with nano-grains of metal materials. At present, according to the function object classification, the surface nanocrystallization has three basic ways^[3]: nanocrystallization by surface coating (or deposition); surface self-nanocrystallization; hybrid surface nanocrystallization. Self-nanocrystallization has mounts of methods, which mainly produce severe plastic deformation and promote grain refinement to the nanometer scale on the surface of the material under the action of external load repeatedly, including Ultrasonic Mechanical Vibration Technology, Supersonic Fine Particles Bombarding (SFPB)^[4], Surface Mechanical Attrition Treatment (SMAT), Surface Rolling, Laser Shot

Peening, etc. However, certain defects exist in some of these devices. Such as surface mechanical attrition treatment, it depends on vibrator to accelerate projectiles to impact on the surface. However, the projectile's velocity obtained is limited, which makes plastic deformation on the surface insufficient. Meanwhile, geometric shape of workable sample is relatively narrow and simple. Supersonic particle bombardment technology equipment is complex and expensive. The gun, carried the airflow and particle, is core components of super sound speed device. The strict design and material requirements and existence of unstable speed situation makes the technical equipment exist a certain distance from industrial production.

In view of the existing surface nano-technologies having many problems such as complex devices structure, small processing area and long processing time, etc, this paper proposes a new surface self-nanocrystallization devices, namely the Rotational Accelerated Shot Peening (RASP) surface treatment equipment. The technology uses turbine to accelerate projectiles to impact on the surface with a certain speed continuously, which produces strong plastic deformation in the surface to reach the purpose of grain refinement. This method is simple, safe and reliable with low cost of materials and equipment.

Mechanical properties of metallic materials improve after surface self-nano crystallization, such as strength,

hardness, wear resistance and corrosion resistance [5]. In this paper, by using RASP technique, gradient ultra-fine grained surface layer with a certain thickness was prepared for 6063 aluminum alloy. Moreover, optimum production technology parameters were obtained by changing the process parameters and orthogonal testing designation. The microstructure evolutions of the deformed surface layers were performed by TEM and other testing technology. The mechanical properties of samples were analyzed by means of portable roughness tester and hardness testing device.

2 Materials and Method

2.1 Experimental raw material

The experiment was performed on the 6063 aluminum alloy. The chemical composition is listed in table 1. Before processing, the sample surface use metallographic sandpaper for grinding to flat, and clean the surface with acetone and alcohol. Figure 1 is a metallographic image of original structure of 6063 aluminum alloy. as you can see from the picture, the grain boundaries of original sample are obvious, and distribution of grain size is uniform. The average size is about hundreds of micrometers, which means the original structure belongs to coarse grain structure.

Table 1 Chemical Composition of 6063 aluminum alloy (unit: wt%)

Component	Si	Fe	Cu	Mn	Mg	Cr	Zn	Ti	Ni	Al
Content	0.38	0.17	0.02	0.01	0.70	0.01	0.01	0.02	0.01	Allowance



Figure 1 A metallographic image of original structure of 6063 aluminum alloy

2.2 Experimental installation

In this paper, the experimental installation is researched and developed by the research group of teachers and nanjing suinuo nano science and technology co., LTD., called Rotational Accelerated Shot Peening. RASP experiment is a method of self-nanocrystallization/ultrafine crystallization. The experiment equipment includes a workpiece room, steel projectile conveying system, shot peening host. Experimental schematic diagram is shown in Figure 2 The workpiece room: the sample in the workpiece chamber is fixed with clamping system. Clamping

system can adjust the angle of the workpiece deflection institution to make the repeated impact more uniform. Steel projectile conveying system: using conveyor rubber belt, the system transmits projectiles to shot peening system; Shot peening system: the motor is used to drive the rotation of the impeller, blades of which accelerate projectiles to impact on the metal surface with a high speed under the action of centrifugal force. Severe plastic deformation occurs on the surface, finally leading to grain refinement. Velocity of projectiles depends on the speed of motor. The inferent energy can be controlled through changing the speed of motor, diameter of projectiles and processing time.

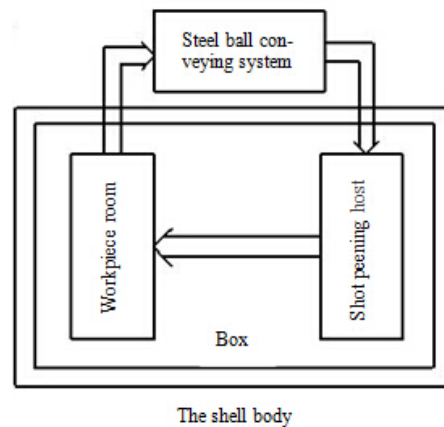


Figure 2 Experimental schematic RASP diagram (include the workpiece room, steel projectile conveying system, shot peening host)

Compared with the existing technology, rotational accelerated shot peening equipment has its significant advantages: (1) Simple structure. The design does not contain complex components, such as vibration device, which only consists of general motors and circulatory system. It is simple and compact structure, and convenient in installation, debugging and maintenance of the equipment. (2) High processing efficiency. This method make projectiles get kinetic energy by using the centrifugal acceleration device, so as to continuously hit the metal plate. The circulation system of the apparatus can convey a plurality of projectiles and it can be reused, which results in multiple bombardment on the surface in a unit of time and reducing the processing time. Compared with the above-mentioned methods of the surface nano-crystallization, the device increases single work area, reduces processing time, and improves work efficiency. (3) A wide range of samples' dimension. The equipment for processing multiple shaped materials, such as flat, circular arc shape or complex interface and other artifacts. This device can also process a variety of component materials, such as pure copper and 6063 aluminum alloy, steel hull, X80 pipeline steel, alloy steel, stainless steel, etc.

2.3 Experimental method

The specimens were processed by the RASP equipment. In order to find the optimal processing parameters with which the better properties can be obtained, in this paper, we make several groups of experiments with the orthogonal experimental design, and discuss the effect of parameters on the numerical results.

Orthogonal experimental design is a method of using orthogonal table to arrange and analyze multiple factors experiment. In all level combination of test factors, we select some representative horizontal combination to experiment, then comprehensively understand test situation through this part of the test results, finally find out the optimal combinations of levels [6].

The experimental design index are roughness and hardness. The roughness value is as small as possible, while the higher the hardness is, the better it will be. There are three factors: the projectile's diameter, the velocity of projectile and processing time, without the interaction among various factors. Each level of influence factors are unequal, 2, 3 and 4, respectively, so we use mixed orthogonal table $L_{24}(2^{13} \times 3 \times 4)$, orthogonal header design as shown in table 2.

The projectile materials of the experiment is high precision rolling bearing steel GCr15. the specific processing parameters are the projectile's diameter (unit: mm), the velocity of projectiles (m/s)

and processing time (min). A total of experiments are 24 groups. All experimental parameters are shown in table 2. These parameters are all a factor regarded as a variable, two other factors remaining unchanged, to reflect the relationship between them.

3 Experimental results and analysis

The roughness of deformed coarse grained aluminum was measured by a portable surface roughness tester RTP-220. The micro-hardness was tested by HMV-G21 micro-hardness tester, using static indentation method. Measuring hardness variation along the depth direction, the load is 98.07mN, the loading time is 10 s. TEM samples were prepared by mechanical grinding, then ion thinning. Tecnai G220 S-TWIN transmission electron microscope (six lanthanum boride) was used to analyze microstructure of samples after treatment.

3.1 Roughness and Hardness

The roughness and hardness is analyzed by using the method of orthogonal experiment to discuss the results in 24 groups of experiments. To analyze the experimental results, It is necessary to calculate the value of K (K is sum of the same level), k value (The average value of each factor of the same level) and range value R [6]. According to the k values, we can

Table 2 Table of orthogonal test designing (three factors without interaction and the corresponding level)

The experimental parameters	
3mm,10m/s,5min	5mm,10m/s,5min
3mm,10m/s,15min	5mm,10m/s,15min
3mm,10m/s,30min	5mm,10m/s,30min
3mm,10m/s,60min	5mm,10m/s,60min
3mm,15m/s,5min	5mm,15m/s,5min
3mm,15m/s,15min	5mm,15m/s,15min
3mm,15m/s,30min	5mm,15m/s,30min
3mm,15m/s,60min	5mm,15m/s,60min
3mm,25m/s,5min	5mm,25m/s,5min
3mm,25m/s,15min	5mm,25m/s,15min
3mm,25m/s,30min	5mm,25m/s,30min
3mm,25m/s,60min	5mm,25m/s,60min

Table 3 The experimental parameters(the projectile's diameter (unit: mm), the velocity of projectiles; (m/s) and processing time(min)

FactorsLevel No.	The projectile's diameter (mm)A	The projectile's velocity (m/s)B	Processing time (min)C
1	3	10	5
2	5	15	15
3		25	30
4			60

Table 4 Analysis and results (ascertain primary and secondary order, optimal levels, optimal combination)

	Experiment No.		Factors			
	1—24	A	B	C		
Roughness	k_1	200.4	174.6	229.6		
	k_2	205.6	125.9	264.1		
	k_3		309.8	164.9		
	k_4			154.4		
	R	5.2	183.9	110.7		
	Primary and secondary order			B>C>A		
	Optimal levels			A_1	B_2	C_4
Optimal combination			$A_1B_2C_4$			
Hardness	k_1	67.2	66.6	68.2		
	k_2	68.4	66.7	71.3		
	k_3		71.03	61.6		
	k_4			67.5		
	R	1.2	7.3	9.7		
	Primary and secondary order			C>B>A		
	Optimal levels			A_2	B_3	C_2
Optimal combination			$A_2B_3C_2$			

determine the optimal level, and select the optimal combination. Primary and secondary order of factors are based on the value of R. The larger values of R is, the more influence on experimental index the change level of the factor has. indicates the factor more important. The analysis and results are shown in table 3.

In conclusion, the best process parameters tentatively are summarised as follows: a) the roughness: 3mm, 15m/s, 60min; b) the hardness: 5mm, 25m/s, 15min. Overall balance determine the optimal process conditions. According to the factors of primary and secondary, optimization of conditions of the above two indexes isolate inconsistencies must be comprehensive consideration to determine the optimum process conditions. For factor B, the excellent level is B_2 for the effect on roughness, which is the primary factor. While for the influence on hardness, the optimal level is B_3 , which is the secondary factor for it. If the level B_2 is selected, the roughness is 172% lower than that in B_3 . While the hardness value is similar, so level B_2 is choose as the optimal level. Factor C, it is the secondary factor for influence on the roughness, the primary factor for effect on the hardness. When the main consideration is roughness, the optimal level is C_4 , on the contrary, the optimal level is C_2 . If C_2 is selected, the roughness nearly two times higher than that in C_4 , while the hardness value is similar. as a result, for factor C, the optimal level is C_4 . The factor A, its effect on the roughness and hardness are not significant. In the condition of B_2 to be taken for factor and C_4 to be taken for factor C, the roughness in A_2 is 42% higher than that in A_1 , while the hardness increase by 3%, so the optimal level is A_1 for factor

A. To sum up, the best process parameters are shown as follows: 3mm, 15m/s, 60min.

3.1.1 The roughness results and analysis

Table 4 shows that for the roughness, the primary and secondary order of Impact factors is B>C>A, that is to say, B is the main factor, C is a minor factor, and A is unimportant factor. Figure 3 is a diagram of roughness. Figure 3 a) is a diagram of the projectile velocity regarded as a variable. The figure shows ceteris paribus, the surface roughness value is lager with projectile velocity increasing. When process parameters are 3mm, 10m/s, 5min, the surface roughness value reaches to minimum, about 96 μm . While parameters are 5mm, 25m/s, 60min, the surface roughness is minimal, about 424 μm . When the diameter of projectile is 3mm, projectile velocities are 10m/s, 15m/s, 25m/s respectively, the surface roughness of the samples was less than 200 μm , that is to say, the sample surface is neat, which is similar to the situation of projectile diameter 5mm, projectile velocity 10 m/s, 15 m/s. While projectile diameter is 5 mm, and projectile velocity is 25 m/s, the surface roughness increases obviously, namely, the sample surface is more uneven. Figure 3 b) is diagram of processing time regarded as a variables. From the figure, ceteris paribus, the sample surface is more uneven with increasing of processing time. When process parameters are 3 mm, 15 m/s, 60 min, the surface roughness value is about 160 μm , namely, the sample surface is relatively flat. When processing time sustains constant, the surface roughness of parameters for 5mm, 25m/s is far higher than the other parameters. The possible reason may be that as the experiment carried out, the projectile energy continues to increase, the surface deformation work increases, dynamic recovery occurs to soften it,

which means continuous impact on the sample surface will make its surface pits increasing, finally the surface roughness becomes higher. Figure 3 c) is a diagram of projectile diameter regarded as a variable. It can be seen from the figure that ceteris paribus, the surface roughness value is higher with projectile diameter increasing. When the process parameters are 25 m/s, 15min, the surface roughness of projectile diameter of 5 mm (200 μm) is almost double that of projectile diameter of 5 mm (120

μm). In the same situation, When the process parameters are 25 m/s, 60min, the surface roughness of projectile diameter of 5 mm (424 μm) is much higher than that of projectile diameter of 5 mm (200 μm), that is to say, smaller projectiles will lead to flat surface^[7]. This phenomenon is similar to the electric spark line cutting relationship between energy and roughness, i.e., the surface roughness increases correspondingly with the cutting speed^[8].

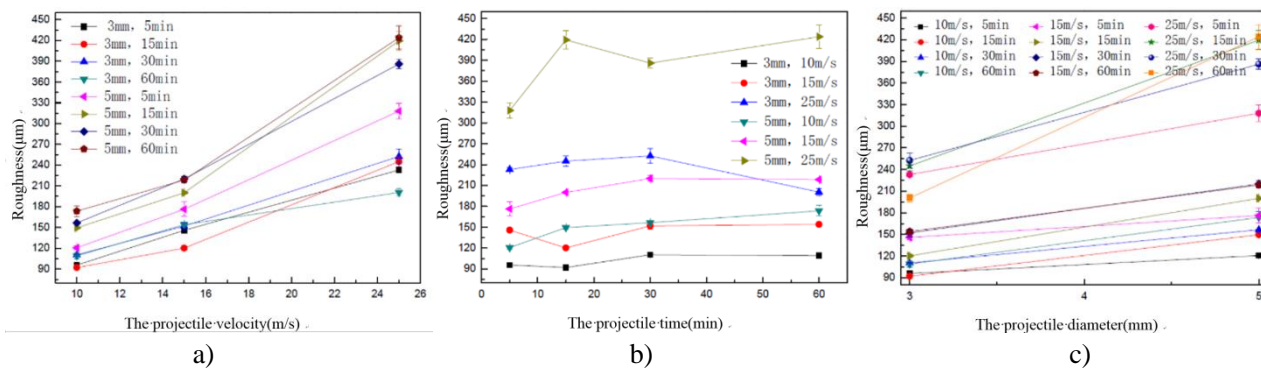


Figure 3 Diagrams of roughness. a) projectile velocity regarded as a variable; b) projectile processing time regarded as a variable; c) projectile diameter regarded as a variable

3.1.2 The micro-hardness results and analysis

Table 4 shows that for the micro-hardness, the primary and secondary order of Impact factors is $C > B > A$, that is to say, C is the main factor, B is a minor factor, and A is unimportant factor. Figure 4 is a diagram of micro-hardness. Figure 4 (a), (b) are diagrams of projectile velocity regarded as a variable. The figure shows ceteris paribus, the hardness values are larger with projectile velocity increasing. In figure 4 (c), processing

time is treated as a variable. The figure shows when the projectile diameter is 5 mm, the micro-hardness of gradient structure increases and then decreases with processing time increasing, that is, there exists a critical value. When Processing time increases to 60 min, micro-hardness reduced, the reason of which may be temperature of the sample rises during RASP treating process, leading to dynamic recrystallization in the surface, then making grain growth occur^[9].

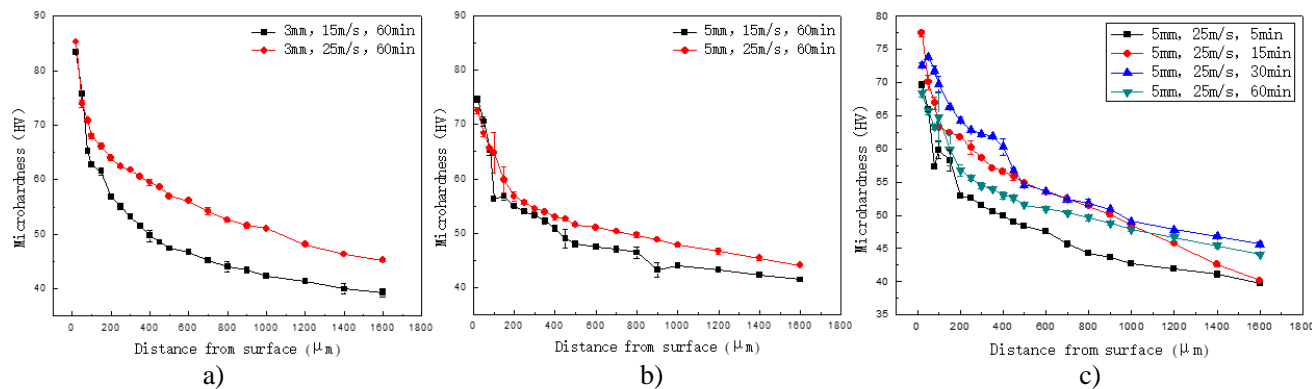


Figure 4 Diagrams of hardness. a) projectile velocity regarded as a variable (3mm,15m/s, 25m/s, 60min); b) projectile velocity regarded as a variable (3mm, 15m/s, 25m/s,60min); c) processing time regarded a sa variable (3mm, 25m/s, 5min,15min, 30min, 60min)

Figure 5 are diagrams of projectile diameter regarded as a variable. The figure shows ceteris paribus, namely 15m/s, 60min, two kinds of topmost surface hardness are close. While the projectile velocity is 25m/s, and processing time is 60min, the sample surface hardness with the projectile diameter of 3 mm is larger than the diameter of 5mm. This is probably because

recrystallization or grain growth may occur in the surface layer, resulting in lower hardness^[10]. It requires subsequent experiments for further certification. Figure 4 and figure 5 show that the micro-structure treated by RASP is gradient structure, namely, the hardness value decreases along the vertical section from surface to matrix. At the same time, the surface micro-hardness

increases significantly [11]. When the process parameters are 3mm/5mm, 15m/s, 60min, micro-hardness of two samples are similar, but we can see from Figure 3, the surface roughness value of former specimen is much smaller than the latter. When the process parameters are 5mm, 25m/s, 15min, 30min and 60min, the surface hardness of the former sample is much larger than the latter, the reason of which may be that as the experiment keep going, the deformation in the surface becomes more several, and dynamic recrystallization produced, leading to grain growth in the surface layer, which results in lower hardness, conforming to the Hall-Petch relationship [12]. Through the above analysis, the optimal process parameters are 3 mm, 15 m/s, 60min, which is consistent with the analysis of orthogonal experiment.

In summary, there is a critical value of the projectile energy. When the projectile energy is lower than this value, the upper the projectile energy is, the higher the hardness value is. Because under the action of external force, plastic deformation occur on the surface, which leads to dislocation slip, appreciation, tangle ,resulting in grain refinement in the surface layer, showing hardness decrease. Plastic deformation carries on, which is conducive to improve the hardness of the metal [13]. When the projectile energy is higher than this value, the upper the projectile energy is, the smaller the hardness value is. Because exorbitant energy causes dynamic recrystallization in the surface layer, resulting in grain growth and hardness decrease.

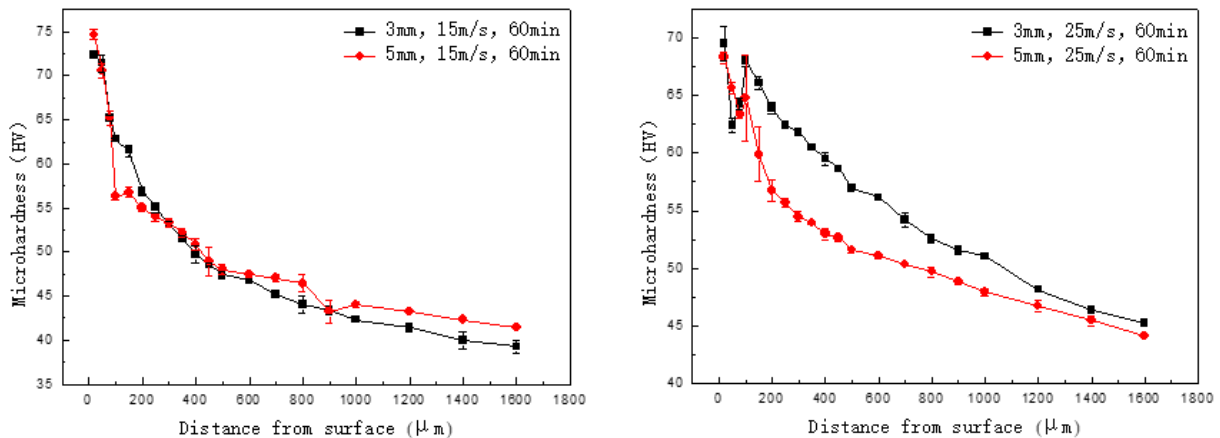
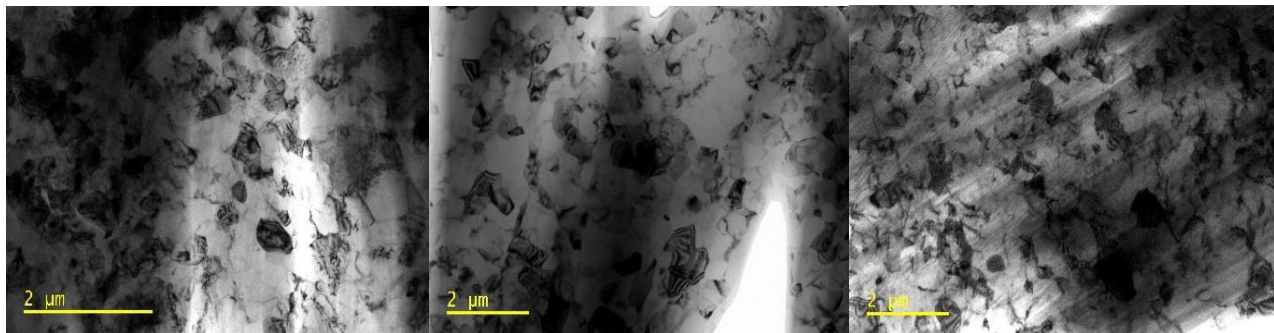


Figure 5 Diagrams of hardness with projectile diameter regarded as a variable. a) 3mm, 5mm, 15m/s, 60min; b) 3mm,5mm, 25m/s, 60min

3.2 TEM results and analysis

The microstructure of surface layer treated by RASP (plane sample: the topmost surface , splicing sample: vertical section) can be observed by using TEM experiment. According to images of morphology, the average grain size of vertical section along the topmost surface to the matrix can be kept statistics.

Figure 6 shows TEM bright field images of topmost surface in 6063 aluminum alloy treated by RASP treatment with different parameters. It is shown that after RASP treatment, grain refinement is obvious, grain orientation is random and the grain size of surface layer is respectively about 500 nm (a), 512 nm (b) and 528 nm (c), which means the microstructure is ultrafine structure.



(a) 3mm、15m/s、60min

(b) 3mm、25m/s、30min

(c) 5mm、25m/s、30min

(the experimental parameters are 3mm,15m/s,60min; 3mm,25m/s,30min; 5mm,25m/s,30min, respectively)

Figure 6 TEM bright field images of topmost surface in 6063 aluminum alloy treated by RASP treatment.

Figure 7 shows TEM bright field images of gradient structure in 6063 aluminum alloy treated by RASP

treatment along vertical section from topmost surface to about 150 μm (3mm, 25m/s, 60min), 150 μm (5mm, 25m/s, 15min), 300 μm (5mm, 25m/s, 30min) depth. From the figures, we can see, after RASP treatment, grain refinement in the surface layer is obvious, and with the depth increasing from the surface, the grain size increases, showing obvious gradient structure. The figure

7 also shows the average grain size of different depth from topmost surface. Through the graph, after RASP processing, the surface layer realizes grain refinement, and experimental evidences show that after the RASP treatment the microstructure of the surface layer may be refined to the ultrafine-scale [14].

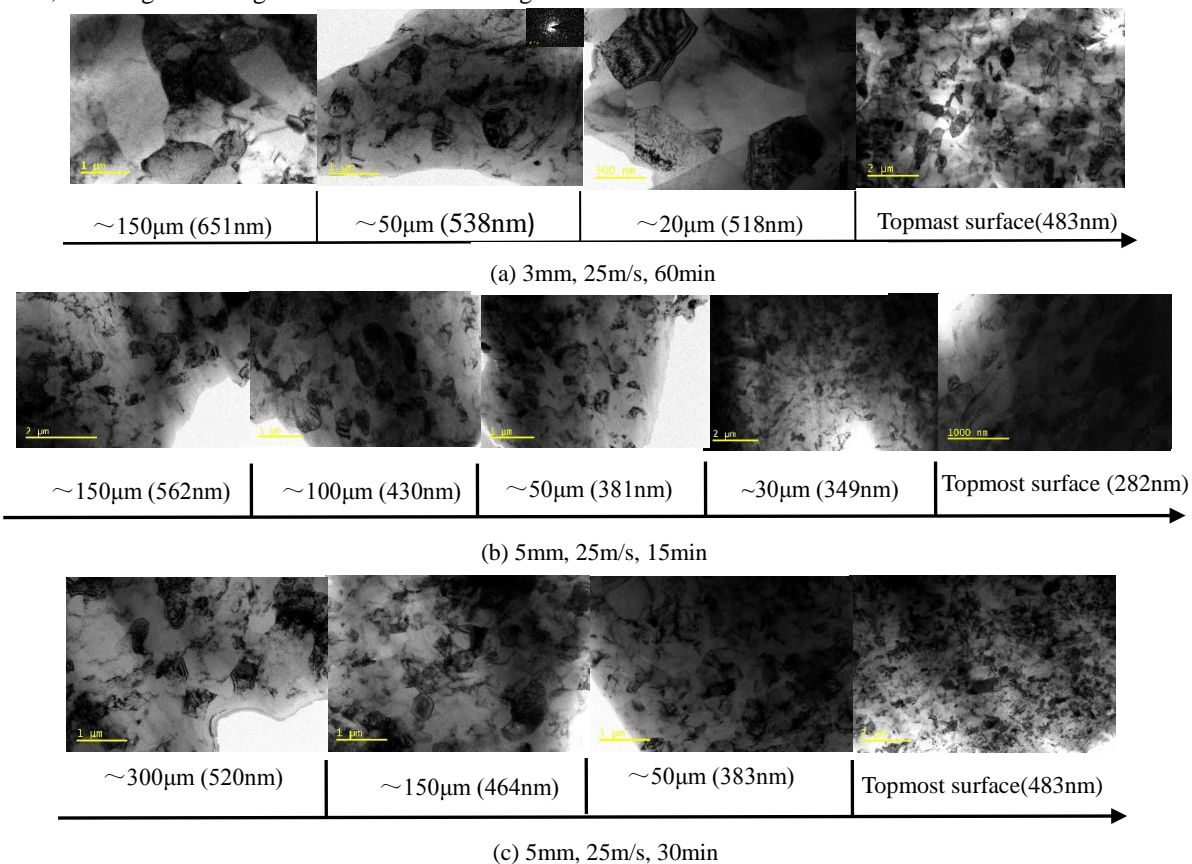


Figure 7 TEM bright field images of gradient structure in 6063 aluminum alloy treated by RASP treatment along vertical section from topmost surface to about 150 μm (3mm, 25m/s, 60min), 150 μm (5mm, 25m/s, 15min), 300 μm (5mm, 25m/s, 30min) depth

Figure 8 shows TEM bright field images of high-density dislocation walls (DDWs) and dislocation tangles (DTs) at the topmost surface in 6063 aluminum alloy treated by RASP treatment.

With the increase of strain, there are more and more dislocations. These dislocations come together, forming high-density dislocation walls and dislocation tangles.

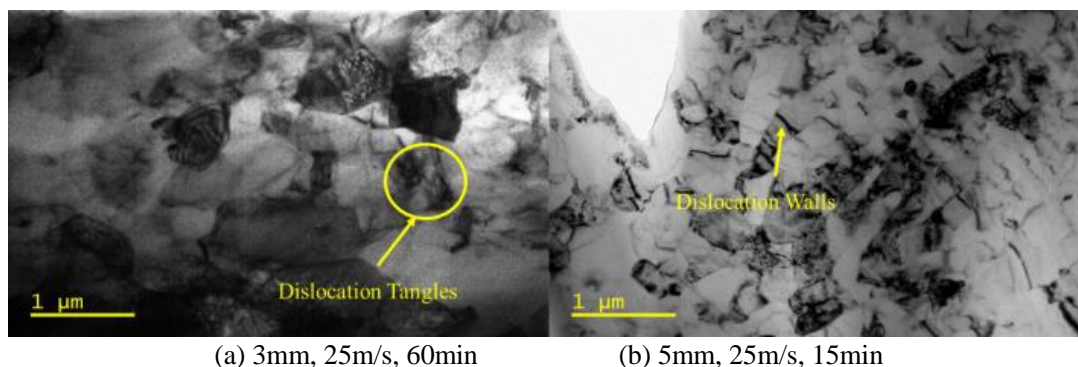


Figure 8 TEM bright field images of high-density dislocation walls and dislocation tangles at the topmost surface

Figure 9 is average grain size of the topmost

surface in 6063 aluminum alloy treated by RASP

treatment. The figure shows that the surface grain size of all the samples are less than 550 nm, which suggests RASP treatment technology achieves grain refinement to ultrafine-scale, and the process parameters for 5mm, 25m/s, 15min reach to the best refinement effect. From the graph, we also can

conclude that, when the projectile diameter and velocity (5mm, 25m/s) are limited, the sample surface grain size is smaller with processing time decreasing. When the projectile diameter and processing time (3mm; 60min) are limited, the sample surface grain size decreases with projectile velocity increasing.

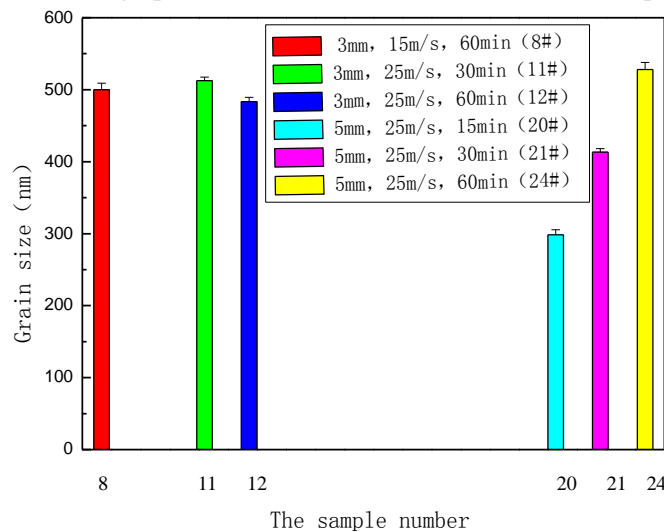


Figure 9 Average grain size of the topmost surface in 6063 aluminum alloy treated by RASP treatment

(the experimental parameters are 3mm,15m/s,60min; 3mm, 25m/s, 30min; 5mm, 3mm, 25m/s, 60min; 5mm,25m/s, 15min; 5mm, 25m/s, 30min; 5mm, 25m/s,60min, respectively)

The above analysis shows that plastic deformation occurs in the surface layer during RASP processing, producing a large number of dislocations, forming a high density of dislocations and dislocation tangles wall, which changes the grain boundary and then converts to large angle sub-grain boundary by constantly absorbing dislocations. Coarse grains refine to subgrains through the above process, which is repeated, achieving grain refinement. With the projectile energy (associated with the projectile diameter and speed) increasing, grain refinement increases then decreases. The reason of decrease may be it is easy for dislocations to be absorbed in higher temperature, which results in a dynamic recovery, decrease of density of dislocations, increase of grain boundary misorientation, leading to the large angle grain boundary percentage and the average misorientation increasing^[15]. Therefore, for the metals with high stacking fault energy, dynamic recovery hinders the processing of grain refinement.

4 Conclusions

In this paper, using metallographic microscope, TEM and other testing technology analyzes the microstructure and microstructure change in 6063 aluminum alloy treated by RASP treatment and preliminary study of micro-mechanism of grain refinement. Portable roughness tester and hardness tester are used to measure the surface properties. The

experimental conclusions are as follows:

(1) When projectile velocity regarded as a variable, the figure shows *ceteris paribus*, the surface roughness value and hardness is larger with projectile velocity increasing; Projectile diameter regarded as a variable, *ceteris paribus*, namely 15m/s, 60min, two kinds of topmost surface hardness are close. While the surface roughness value is higher with projectile diameter increasing; Processing time treated as a variable, when the parameters are 5 mm, 25m/s, the micro-hardness of gradient structure increases and then decreases with processing time increasing, that is, there exists a critical value.

(2) While the sample surface is more uneven with increasing of processing time. With all that said, the optimum process parameters is 3mm, 15m/s, 60min, which can achieve higher hardness and flatter surface.

(3) 6063 aluminum alloy is FCC structure with high stacking fault energy. Under the external loads, it has severe plastic deformation in the surface layer, which leads to dislocation movement, forming high-density dislocation walls (DDWs) and dislocation tangles (DTs). Through gradually absorbing dislocations, dislocation walls and dislocation tangles evolves to small angle sub-grain boundaries; small angle sub-grain boundaries continue to absorb dislocations to form large angle grain boundaries; The above process is repeated in sub-grain, leading to the grain size decrease, the misorientation increase, and finally equiaxed and randomly oriented

ultrafine grains are obtained. The surface hardness increase is mainly due to work hardening and grain refinement strengthening effect.

Acknowledgements: This research used the resources of the Nanjing University of Science and Technology analytical and testing center. This research was funded by NSFC (Grant No. 51301092) and the National Key R & D Program of China (Grant No. 2017YFA0204403). Open Research Fund of Science and Technology on High Strength Structural Materials Laboratory (No. O2016006).

References

- [1] K LU, J LU. Nanostructured surface layer on metallic materials induced by surface mechanical attrition treatment[J]. Mater. Sci. Eng. A, 2004, 10(3):38-45.
- [2] K LU, J LU. Surface Nanocrystallization (SNC) of Metallic Materials Presentation of the Concept behind a New Approach [J]. Mater. Sci. Technol, 1999, 15(3):193-197.
- [3] Liu G, Yong X P, Lu K. Surface nanocrystallization In Metal and Its Present [J]. China Surface Engineering, 2001, 52(3): 1-5
- [4] Ba D M, Ma S N, Li C Q. Surface nanocrystallization Research In Supersonic Particles Bombard the Surface of 45 # steel[J]. Journal of materials science and technology, 2007, 15 (3): 342-342.
- [5] F. J. Humphreys. A unified theory recovery, recrystallization and grain growth, based on the stability and growth of cellular microstructure. The base model [J]. Acta mater, 1997, 45(10): 4231-4240.
- [6] L Liu, P Y Li. Orthogonal experiment and optimization of heat treatment process of the 34CrNi3Mo steel [J]. Material heat treatment technology, 2011, 1(6):164-166.
- [7] K. Dai, J. Villegas, Z. Stone, L. Shaw. Finite element modeling of the surface roughness of 5052 Al alloy subjected to a surface severe plastic deformation process [J]. Acta Materialia, 2004, 52: 5771-5782.
- [8] L Yang, A J Cai. Research on WEDM Process Parameters on the effects of the machining speed and surface roughness [J]. Machine tools and hydraulics, 2011, 39(15):45-47.
- [9] H Liu. Research status of metal material surface nanocrystallization [J]. Petroleum engineering construction, 2010, 36(3):11-15.
- [10] G Y Qiao, Q P Sheng. The research status of metal surface self nanocrystallization by application of ultrasonic [J]. Oral material equipment, 2011, 20(2):101-105.
- [11] J C Villegas, L L Shaw. Nanocrystalline process and mechanism in a nickel alloy subjected to surface severe plastic deformation [J]. Acta Materialia, 2009, 57: 5782-5795.
- [12] Farahbakhsh I, Zakeria A, Manikandan P, Evaluation of Nanostructured coating layers formed on Ni projectiles during mechanical alloying of Cu powder [J]. Applied Surface Science, 2010, 358: 2354-2359.
- [13] Romankov S, Komarov S V. Fabrication of TiN coatings using mechanical milling techniques [J]. Int. J. Refract. Met. Hard Mater, 2009, 27: 492-497.
- [14] Xu C, Horita Z, Langdon T G. Microstructural Evolution in 6063 aluminum alloy uniaxial in the Early Stages of Processing by High-Pressure Torsion [J]. Materials transactions, 2010, 51(1): 2-7.
- [15] K. Wang, N.R. Tao, et al. Plastic strain-induced grain refinement at the nanometer scale in copper [J]. Acta Materialia, 2006, 54: 5281-5291.